

**REPORT DOCUMENTATION PAGE**

Form Approved  
OMB No. 0704-0188

The public reporting burden for this collection of information is estimated to average 1 hour per response, including the time for reviewing instructions, searching existing data sources, gathering and maintaining the data needed, and completing and reviewing the collection of information. Send comments regarding this burden estimate or any other aspect of this collection of information, including suggestions for reducing the burden, to the Department of Defense, Executive Service Directorate (0704-0188). Respondents should be aware that notwithstanding any other provision of law, no person shall be subject to any penalty for failing to comply with a collection of information if it does not display a currently valid OMB control number.

**PLEASE DO NOT RETURN YOUR FORM TO THE ABOVE ORGANIZATION.**

|   |             |  |   |  |  |
|---|-------------|--|---|--|--|
| <b>1. REPORT DATE (DD-MM-YYYY)</b><br>01-6-2012   |             | <b>2. REPORT TYPE</b><br>Master's Thesis |   | <b>3. DATES COVERED (From - To)</b><br>JAN 2012 - JUN 2012 |  |
| <b>4. TITLE AND SUBTITLE</b><br>Fracture and Plasticity Characterization of DH-36 Navy Steel  |             |  |   | <b>5a. CONTRACT NUMBER</b><br>N00244-09-G-0014             |  |
|   |             |  |   | <b>5b. GRANT NUMBER</b>                                    |  |
|   |             |  |   | <b>5c. PROGRAM ELEMENT NUMBER</b>                          |  |
| <b>6. AUTHOR(S)</b><br>Christopher MacLean  |             |  |   | <b>5d. PROJECT NUMBER</b>                                  |  |
|   |             |  |   | <b>5e. TASK NUMBER</b>                                     |  |
|   |             |  |   | <b>5f. WORK UNIT NUMBER</b>                                |  |
| <b>7. PERFORMING ORGANIZATION NAME(S) AND ADDRESS(ES)</b><br>Massachusetts Institute of Technology  |             |  |   | <b>8. PERFORMING ORGANIZATION REPORT NUMBER</b>            |  |
| <b>9. SPONSORING/MONITORING AGENCY NAME(S) AND ADDRESS(ES)</b><br>Naval Postgraduate School<br>Monterey, CA 93943   |             |  |   | <b>10. SPONSOR/MONITOR'S ACRONYM(S)</b><br>NPS             |  |
|   |             |  |   | <b>11. SPONSOR/MONITOR'S REPORT NUMBER(S)</b>              |  |
| <b>12. DISTRIBUTION/AVAILABILITY STATEMENT</b><br>1. DISTRIBUTION STATEMENT A. Approved for public release; distribution is unlimited.  |             |  |   |  |  |
| <b>13. SUPPLEMENTARY NOTES</b>  |             |  |   |  |  |
| <b>14. ABSTRACT</b><br>Multi-layered plates consisting of DH-36 steel coated by a thick layer of polyurea, for increased blast and impact protection, are of increasing importance to the Department of Defense. A hybrid approach of experiments and simulation was performed to characterize fracture and plasticity of DH-36 Navy steel, which is the first step in creating an accurate model of the composite material. The performance limit to this material during an impact is ductile fracture. The prediction follows that the onset of fracture occurs when a certain critical value of plastic strain is reached. This value is highly dependent on the state of stress. |             |  |   |  |  |
| <b>15. SUBJECT TERMS</b>  |             |  |   |  |  |
| <b>16. SECURITY CLASSIFICATION OF:</b>  |             |  | <b>17. LIMITATION OF ABSTRACT</b><br><br>UU | <b>18. NUMBER OF PAGES</b><br><br>99                       | <b>19a. NAME OF RESPONSIBLE PERSON</b><br>Julie Zack               |
| a. REPORT   | b. ABSTRACT | c. THIS PAGE                             |   |  | <b>19b. TELEPHONE NUMBER (Include area code)</b><br>(831) 656-2319 |

Reset

**Fracture and Plasticity Characterization of DH-36 Navy Steel**

by

CHRISTOPHER GLENN MACLEAN

B.S. Mechanical Engineering  
Tulane University, 2007

Submitted to the  
DEPARTMENT OF MECHANICAL ENGINEERING

In Partial Fulfillment of the Requirements for the Degrees of

NAVAL ENGINEER  
and  
MASTER OF SCIENCE IN MECHANICAL ENGINEERING

at the  
MASSACHUSETTS INSTITUTE OF TECHNOLOGY  
June 2012

**© 2012 Christopher MacLean. All rights reserved.**

The author hereby grants to MIT permission to reproduce and to distribute publicly paper and electronic copies of this thesis document in whole or in part in any medium now known or hereafter created.

Signature of Author: \_\_\_\_\_  
Department of Mechanical Engineering  
May 1, 2012

Certified by: \_\_\_\_\_  
Tomasz Wierzbicki  
Professor of Applied Mechanics  
Thesis Supervisor

Accepted by: \_\_\_\_\_  
David E. Hardt  
Ralph E. and Eloise F. Cross Professor of Mechanical Engineering  
Chair, Department Committee on Graduate Students

# Fracture and Plasticity Characterization of DH-36 Navy Steel

By

CHRISTOPHER G. MACLEAN

Submitted to the Department of Mechanical Engineering on May 1, 2012 in Partial Fulfillment of the Requirements for the Degree of Naval Engineer and Master of Science in Mechanical Engineering

## ABSTRACT

Multi-layered plates consisting of DH-36 steel coated by a thick layer of polyurea, for increased blast and impact protection, are of increasing importance to the Department of Defense. A hybrid approach of experiments and simulation was performed to characterize fracture and plasticity of DH-36 Navy steel, which is the first step in creating an accurate model of the composite material. The performance limit to this material during an impact is ductile fracture. The prediction follows that the onset of fracture occurs when a certain critical value of plastic strain is reached. This value is highly dependent on the state of stress.

Seven different types of tests were performed, including tensile tests on dog-bone and notched specimens and punch indentation tests on circular blanks. Also, tensile and shear tests were performed on butterfly specimens using the dual actuator loading frame. Fracture surface strains were measured using digital image correlation. Local fracture strains were obtained by using an inverse engineering method of matching measured displacement to fracture with computer simulations. The results are used to calibrate the Modified Mohr Coulomb fracture model which is expressed by the stress state invariants of Lode angle and triaxiality.

Thesis Supervisor: Tomasz Wierzbicki

Title: Professor of Applied Mechanics

## Table of Contents

|       |  |    |
|-------|--|----|
| 1     | Introduction and Overview .....                | 8  |
| 1.1   | Motivation and Objective .....                 | 8  |
| 1.2   | Modified Mohr Coulomb (MMC) Model.....         | 8  |
| 1.3   | DH-36 Steel and Polyurea .....                 | 11 |
| 2     | Experimental Testing Program.....              | 13 |
| 2.1   | Equipment.....                                 | 13 |
| 2.1.1 | MTS and Instron.....                           | 13 |
| 2.1.2 | Digital Image Correlation (DIC) .....          | 14 |
| 2.2   | Specimens .....                                | 16 |
| 2.2.1 | Dog-bone Specimen.....                         | 17 |
| 2.2.2 | Notched and Hole Specimens .....               | 21 |
| 2.2.3 | Punch Specimen.....                            | 22 |
| 2.2.4 | Butterfly Specimen.....                        | 23 |
| 3     | Numerical Simulation.....                      | 24 |
| 3.1   | Hybrid Approach .....                          | 24 |
| 3.2   | Setup .....                                    | 24 |
| 3.3   | Validation .....                               | 26 |
| 3.4   | Data Analysis .....                            | 31 |
| 3.5   | New Shear Specimen .....                       | 33 |
| 4     | Modified Mohr-Coulomb Fracture Criterion ..... | 34 |
| 4.1   | Data Collection and Calibration .....          | 34 |
| 4.2   | New Shear Specimen Discussion .....            | 37 |
| 4.3   | Damage Evolution (Accumulation) .....          | 39 |
| 4.4   | Fracture Parameters and Fracture Locus.....    | 39 |
| 4.4.1 | 2D Plane Stress Model .....                    | 41 |
| 4.4.2 | 3D Fracture Locus.....                         | 41 |
| 5     | Conclusions and Further Studies .....          | 43 |
|       | References .....                               | 44 |
|       | Appendix A: Theory – Stress States .....       | 48 |
|       | Appendix B: Additional Data.....               | 51 |

## **Acknowledgements**

The author thanks the following individuals for their assistance in completing this thesis:

Professor Wierzbicki for his direction and guidance on this project.

My colleagues in the Impact and Crashworthiness Lab (ICL), Kirki Kofiani, Evangelos Koutsolelos, Allison Beese, Meng Luo, Stephane Marcadet and Matthieu Dunand for all their assistance.

CAPT Mark Welsh, CAPT Mark Thomas and CDR Pete Small for their leadership of the 2N program during my three years at MIT.

Dr. Willis Mock of NSWC Dahlgren for providing the material for testing.

## List of Figures

|  |    |
|--|----|
| Figure 1: Example 3D MMC fracture locus (Bai and Wierzbicki 2008). .....   | 9  |
| Figure 2: Dependence of the equivalent strain to fracture on the stress triaxiality (Bao and Wierzbicki 2004). .....   | 9  |
| Figure 3: Conceptual representation of the initial stress states on the plane of $\eta$ and $\theta$ (Y. Bai 2008). ...  | 10 |
| Figure 4: 3D representation of the Johnson-Cook phenomenological fracture model (Wierzbicki and Mohr 2010). .....  | 11 |
| Figure 5: MTS loading frame. ....  | 13 |
| Figure 6: Dual actuator loading frame and system schematic, 1—lower specimen grip, 2—upper grip, 3—upper cross-head, 4—sliding table, 5—vertical load cells, 6—horizontal load cell and actuator, 7—digital camera (Mohr and Oswald 2008). ..... | 13 |
| Figure 7: DIC strain contour plot. ....  | 14 |
| Figure 8: Extensometer placement. ....   | 15 |
| Figure 9: 3-D DIC surface representation of the initial and deformed surface. ....   | 16 |
| Figure 10: ASTM tensile dog-bone specimen (ASTM 2001). ....  | 17 |
| Figure 11: Power law extrapolation. ....   | 18 |
| Figure 12: Dog-bone orientation with respect to the rolling direction. ....  | 19 |
| Figure 13: Average transverse (width) plastic strain versus through-thickness plastic strain for three specimens in each orientation. ....   | 20 |
| Figure 14: Lankford coefficient plot. ....   | 20 |
| Figure 15: Tensile specimens with different notch radii and a central hole (Dunard and Mohr 2010a). ...  | 22 |
| Figure 16: Punch specimen schematic and post test. ....  | 23 |
| Figure 17: Dual Actuator Loading Frame and definition of the bi-axial loading angle $\beta$ (Mohr, Dunard and Kim 2010). ....  | 23 |
| Figure 18: Optimized butterfly specimen (Dunard and Mohr 2009). ....   | 24 |
| Figure 19: Butterfly specimen in tension with a von Mises stress contour plot. ....  | 25 |
| Figure 20: Punch test simulation with equivalent plastic strain (PEEQ in Abaqus) contour plot. ....  | 26 |
| Figure 21: Extensometer placement and matched FE model for the 6.67 notched specimen. ....   | 27 |
| Figure 22: Material plastic behavior. ....   | 27 |
| Figure 23: Force displacement simulation test series for the central hole specimen. ....   | 28 |
| Figure 24: Force displacement simulation comparison for the 6.67 notched specimen. ....  | 29 |
| Figure 25: 3-D DIC displacement contour plot. ....   | 29 |
| Figure 26: Punch test setup and specimen after fracture. ....  | 30 |
| Figure 27: Punch force displacement curve. ....  | 30 |
| Figure 28: Typical stress strain curve. ....   | 31 |
| Figure 29: Fracture evolution in the butterfly specimen in tension. 1-4 show the first four seconds of onset of fracture with a zoomed in image. 5 is taken at a later time to show a clear fracture. ....                                       | 32 |
| Figure 30: Butterfly shear test showing front and back views and highlighting the unwanted edge buckling and fracture. ....  | 32 |
| Figure 31: New Shear Specimen (inches). ....   | 33 |
| Figure 32: Equivalent plastic strain and triaxiality. ....   | 35 |

|   |    |
|---|----|
| Figure 33: Equivalent plastic strain and Lode angle.....  | 36 |
| Figure 34: New shear specimen experiment prior to testing, mid-test, one second prior to fracture, and one second after fracture. ....  | 37 |
| Figure 35: FE simulation PEEQ contour plot at the displacement of fracture, showing the maximum point of equivalent plastic strain in the edge section not the gage section. The face shown is the middle of the specimen. .... | 37 |
| Figure 36: Plots of equivalent plastic strain as a function of triaxiality and Lode angle.....  | 38 |
| Figure 37: Alternate butterfly specimen for future testing. ....  | 38 |
| Figure 38: Effect of $c_3$ on the yield surface (Beese, et al. 2010).....   | 40 |
| Figure 39: DH-36 MMC 3D Fracture Locus. ....  | 42 |
| Figure 40: The coordinate systems in the space of Principal Stresses (Beese, et al. 2010) (Bai and Wierzbicki 2010) .....   | 49 |

## Nomenclature

|                          |                                      |
|--------------------------|--------------------------------------|
| $\eta$                   | Triaxiality                          |
| $\bar{\theta}$           | Lode angle                           |
| $F$                      | Force                                |
| $J_i$                    | Invariants of stress deviator        |
| $A_0$                    | Initial area of gage section         |
| $\Delta L$               | Change in length of extensometer     |
| $L_0$                    | Initial length of extensometer       |
| $\sigma_m$               | Mean stress                          |
| $[\sigma]$               | Cauchy stress tensor                 |
| $\bar{\sigma}$           | Equivalent stress                    |
| $\sigma_{eng}$           | Engineering stress                   |
| $\sigma_t$               | True stress                          |
| $\sigma_n$               | Normal stress                        |
| $\bar{\sigma}_f$         | Equivalent fracture stress           |
| $\tau$                   | Shear stress                         |
| $\varepsilon_{eng}$      | Engineering strain                   |
| $\varepsilon_t$          | True strain                          |
| $\bar{\varepsilon}_f$    | Equivalent fracture strain           |
| $\varepsilon_e$          | Elastic strain                       |
| $\varepsilon_f$          | Fracture strain                      |
| $\varepsilon_{pl}$       | Plastic strain                       |
| $\bar{\varepsilon}_{pl}$ | Equivalent plastic strain            |
| $E$                      | Modulus of Elasticity                |
| $r_\alpha$               | Lankford ratio (parameters)          |
| $R_{ij}$                 | Anisotropic creep stress ratio       |
| $\beta$                  | Bi-axial loading angle               |
| $p$                      | Pressure or First Invariant          |
| $q$                      | Von Mises Stress or Second Invariant |
| $r$                      | Third Invariant                      |
| $\underline{s}$ or $[S]$ | Deviatoric stress tensor             |
| $c_1, c_2$               | Mohr Coulomb material constants      |
| $f_i$                    | Functions                            |
| $v_i$                    | Unit normal vectors                  |

# 1 Introduction and Overview

## 1.1 Motivation and Objective

The benefits of polyurea coating of various materials are being utilized in a growing number of applications. The extent to which this light and cheap material can be employed is yet to be realized. It is widely used as a surface coating in many applications to include water treatment inflow/outflow piping, oil pipelines, concrete structures, bridges, shipboard tanks, rudders, struts, anchors etc. The blast resistance of polyurea coated steel is of increasing importance to the Department of Defense (DoD) (Matthews 2004) (Crane 2004).

Low carbon steel alloys account for the majority of the mass of most modern U.S. naval assets. DH-36 steel is a common structural material used for assets in hostile environments, such as Humvees and naval vessels. DH-36 has been the material of choice for past empirical/numerical studies on composite polyurea/steel structures. For optimum use of the composite material it is necessary to design accurate and inexpensive analysis techniques. The most important input to a finite element analysis program is a correctly calibrated fracture model. Once these materials are characterized finite element (FE) simulations vice expensive experiments can be run to optimize the composite for protection, weight and cost. The first step in this process is applying the most recent developments in fracture mechanics to develop an accurate fracture model for DH-36 steel. Thus, the objective of this thesis is to calibrate the Modified Mohr Coulomb (MMC) fracture model for DH-36 steel. It is important to note that the calibration will not only be useful for analyzing the composite structures but also for stand-alone applications of DH-36 steel.

## 1.2 Modified Mohr Coulomb (MMC) Model

Fracture models can be developed on the microscopic scale with dependence on either the polycrystalline structure of the material or a mechanism basis. A polycrystalline plasticity approach shows promise but is currently lacking in computational efficiency. Mechanism based models are common and predict fracture by the known phenomena of nucleation, void growth and propagation of cracks within ductile materials. These models are based on the work of McClintock (1968) and Rice and Tracey (1969) who showed the void growth as the evolution of spherical and cylindrical holes. Results confirm this mechanism is related to the dimensionless hydrostatic pressure, referred to as stress triaxiality ( $\eta$ ), of the material element. There are a series of these mechanism based models known as Gurson models. Gurson proposed a porous plasticity model based on the quantification of a void volume fraction (Gurson 1977). These models have been popular in industry and academia. They have been repeatedly improved to increase their scope and accuracy (Dunard and Mohr 2010a) (Lassance, et al. 2007) (Wierzbicki and Xue 2005). The problem with these models is that the required material parameters are not measurable using standard experimental techniques (Mohr and Henn 2007). The MMC model used in this paper was proven to yield better results than commonly used mechanism-based Gurson models while at the same time requiring less input parameters (Dunard and Mohr 2010b).

The MMC model uses a phenomenological approach, developed by the Impact and Crashworthiness Lab (ICL) at MIT, to predict ductile fracture. This approach does not model void nucleation and growth

but asserts that fracture occurs when a critical value of equivalent plastic strain  $\bar{\epsilon}_f$  is reached. This critical value will change depending on the stress state, specifically triaxiality and Lode angle ( $\bar{\theta}$ ). The critical value of  $\bar{\epsilon}_f$  can be plotted as a function of  $\eta$  and  $\bar{\theta}$  to create a fracture locus, where any state on or above the created surface signifies a fracture condition in the material (Figure 1).

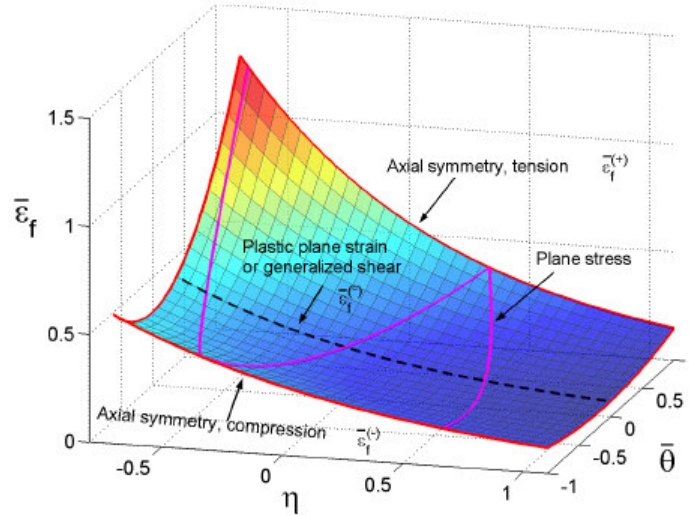


Figure 1: Example 3D MMC fracture locus (Bai and Wierzbicki 2008).

It was shown that the amount of plastic strain a material can withstand before fracture will vary over a large range of stress triaxiality, from  $-1/3$  to 1.1 (Bao 2004). Bao quantified the relation between equivalent plastic strain and triaxiality and showed the function to fall in three distinct branches. Fracture was dominated by the void growth mode in large triaxiality, shear mode for negative triaxiality and a combination of the modes when triaxiality fell between the two regions. The regions are shown in Figure 2.

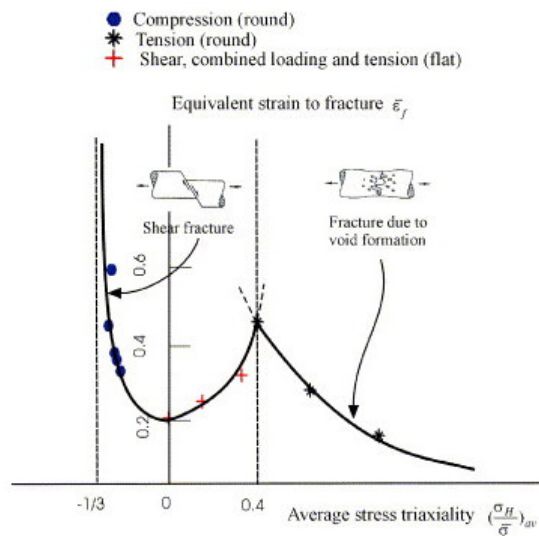


Figure 2: Dependence of the equivalent strain to fracture on the stress triaxiality (Bao and Wierzbicki 2004).

This assertion was enforced through further application and micrographic observations by Mirone (2007). The fracture locus was given a third dimension when Xue and Wierzbicki postulated that the critical value of equivalent plastic strain is a function of triaxiality and the deviatoric state parameter (Wierzbicki and Xue 2005). Previously two invariants (mean stress and equivalent stress) were used to describe pressure dependence of the material. The weighting function was made to include the third invariant of the stress tensor  $J_3$  which introduces the dependence on shear loading into the model (More detail is included in Appendix A). The work of Xue and Wierzbicki established a sound theoretical foundation to the work of Bao and Wierzbicki (Wierzbicki and Xue 2005) (Bao and Wierzbicki 2004). The Mohr-Coulomb (M-C) fracture criteria was revisited by Bai and Wierzbicki because of its explicit dependence on the Lode angle parameter, which was absent in almost all existing ductile fracture models (2010). The local form of the method was transformed/extended to the axes of equivalent strain to fracture ( $\bar{\epsilon}_f$ ), stress triaxiality ( $\eta$ ) and normalized Lode angle ( $\bar{\theta}$ ). The developments led to what is now known as the Modified Mohr-Coulomb (MMC) fracture model. The model is discussed in more detail in section 4.

The parameters of Lode angle and triaxiality are more easily visualized by considering the types of tests used to achieve their specific ranges (Figure 3).

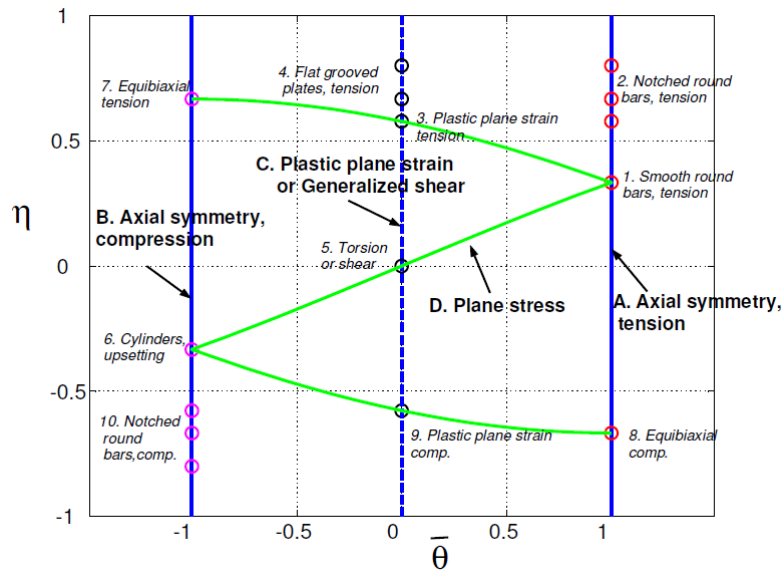


Figure 3: Conceptual representation of the initial stress states on the plane of  $\eta$  and  $\bar{\theta}$  (Y. Bai 2008).

The surface created in the MMC model (Figure 1) is specific to each material. A hybrid approach is used to calibrate the model (Dunard and Mohr 2010a). Each specimen tested (section 2.2) is designed to give a unique Lode angle and triaxiality so that the surface can be extrapolated once the equivalent plastic strain in each test is known. In the physical testing, surface strain fields up to fracture are measured using two and three dimensional digital image correlation (DIC) (section 2.1.2). Due to the localization of plastic deformation, finite element (FE) simulations are performed and validated to obtain the stress and strain histories at the material point where fracture initiates, inside the specimen.

Observing/measuring the behavior at this point in the physical tests would not be practical, thus the

need for valid FE simulations. The simulations are validated using the force displacement curves from the actual tests (section 3.4). Once the simulation results are verified to be accurate they are used to calibrate the model.

### 1.3 DH-36 Steel and Polyurea

DH-36 is characterized by the American Bureau of Shipping (ABS). Detailed information on this high strength carbon steel can be found in the ABS Steel Vessel Rules (Part 2: Rules for Materials and Welding 2012). Polyurea is a type of elastomer which has become popular because of its high toughness, low density, water resistance, fast setting time, and ability to be applied in a spray. There is currently a lot of research focused on DH-36 steel and polyurea. Nemat-Nasser and Guo analyzed the steel over a large range of strain rates and temperatures (Nemat-Nasser and Guo 2003). This initial research is highly referenced in their later work. They applied a physically based (PB) model, grounded on dislocation kinetics, and the Johnson-Cook (JC) phenomenological model (Figure 4) to the material and found good correlation with both (Johnson and Cook 1985). However, the physically based model was superior.

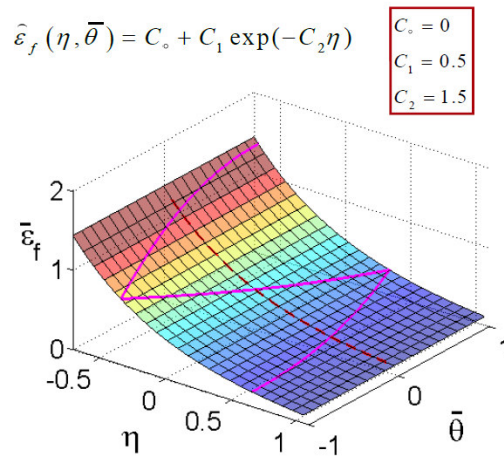


Figure 4: 3D representation of the Johnson-Cook phenomenological fracture model (Wierzbicki and Mohr 2010).

The thermo-visoplastic behavior of the steel was then analyzed by Klepaczko, Rusinek, Rodriguez-Martinez, Pecherski and Arias with the application of the Rusinek-Klepaczko (RK) model, which is also a model with a physical background (Klepaczko, et al. 2009). It was found that the RK model had good agreement with the Nemat-Nassar results and was even more precise than the PB model at high strain rates. Their study reports that the JC model does not consider flow stress as the sum of two parts, the effective stress and “athermal” stress. Also, strain hardening is expressed through a power law that does not take into account strain rate/temperature. As with the JC model, the PB model does not consider strain hardening dependence on strain rate/temperature. The report suggests that the effects of shear banding, a mechanism reported by Nemat-Nasser and Guo (2003), should be incorporated into the finite element simulation. Lastly, the paper concludes that more work needs to be done concerning the failure criterion definition. In their case a simple failure strain level was used.

Sandwiched materials, vice monolithic plates, are also currently a popular topic of study. The main goals are to show that increased energy absorption can be achieved as well as accurate finite

element simulation of the structure. One such study examines a sandwich structure using plates of DH-36 steel tested to simulate a potential blast effect (Nasser-Nemat, et al. 2006). In addition, structures containing an aluminum foam core were analyzed. The plates were modeled using the PB constitutive model described above. A study by Teng, Wierzbicki and Huang looked into ballistic resistance of double layered armor plates of Weldox 460E and Domex protect 500 (Teng, Wierzbicki and Huang 2008). They applied the MMC method and made conclusions targeting a designer, by exploring optimal configurations.

Polyurea is a difficult material to model especially due to its complicated loading-unloading paths (Shim and Mohr 2011a) (Shim and Mohr 2011b). Work is underway modeling composite (sandwich) structures of DH-36 and polyurea. It is a difficult problem to accurately model the materials separately/combined and validate these models while also making useful conclusions on the effects of layer position, thickness, and interface. Work has started analyzing direct-pressure pulse experiments and numerical modeling/simulation (Amini, Simon and Nemat-Nasser 2010a) (Amini, Isaacs and Nemat-Nasser 2010b). In the Amini et al. study(2010a), DH-36 was simulated using the physics-based (PB) model, discussed above. Polyurea was modeled with an experimentally based viscoelastic constitutive model including pressure and temperature sensitivity developed for finite element implementation by Amirkhizi et al. (2006). A follow on paper by Amini and Nemat-Nasser revisits the experiments and analyzes the DH-36 micro-mechanisms of ductile fracturing using an electron microscope (2010c). It reports that the observed ductile fracture involves void nucleation/growth and coalescence creating dimpled fracture surfaces. It also reports no shear-bands develop in or around the fracture surface. Finite element simulations are shown and use the same PB model discussed above. The failure criterion used to simulate the sample failure is a given value of average equivalent plastic strain. Their simulations and experiments show good correlation. The experimental setup and studies are very in-depth. A good follow on study could be testing the failure model on geometries other than a flat plate, changing the stress states.

Comprehensive experimental studies of DH-36 plate and polyurea have also been performed by Naval Surface Warfare Center (NSWC) Dahlgren. Numerical simulations were carried out by a team at Northwestern University with a comparison to the experimental data (Xue, Mock and Belytschko 2010). The DH-36 steel was simulated using a damage plasticity model (L. Xue 2007) (L. Xue 2009). The calibration of the model was done using the stress-strain curve data from Nemat-Nasser and Guo along with an iterative process of comparing simulations to experimental fracture and penetration patterns on flat plates (2003). Similar simulations of experiments conducted at NSWC Dahlgren were carried out by Sayed et al. (2009). The group employed a porous plasticity model for the high strength structural steel (Weinberg, Mota and Ortiz 2006). The model is based off the phenomena of void growth but claims that the constitutive updates provide a “fully variational” alternative to Gurson –like models. The studies by Sayed et al. (2009) and Amani et al. (2010d) point out that more work needs to be done analyzing failure at the interface and delamination.

This paper describes the process of experimentation and simulation on specifically designed specimens in order to accurately define the MMC fracture model over the range of triaxiality, Lode angle, and equivalent plastic strain.

## 2 Experimental Testing Program

### 2.1 Equipment

#### 2.1.1 MTS and Instron

Two loading frames were used during the experimental process. The first of which is a 200kN MTS servo-mechanical loading frame (Figure 5). The frame can be outfit with grips for tension testing and a clamped punch frame for punch indentation testing.

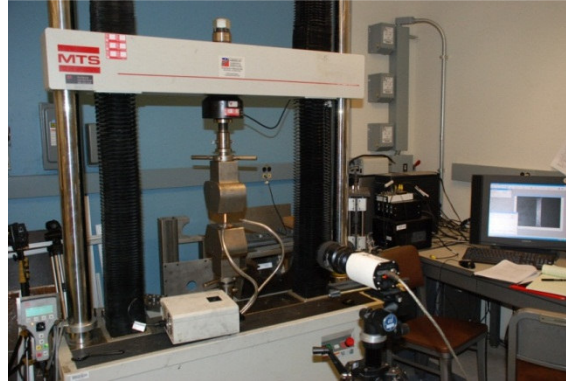


Figure 5: MTS loading frame.

The Instron dual-actuator testing apparatus allows for vertical and/or horizontal motion of the specimen (Figure 6). Almost any loading condition between pure shear and transverse plane strain tension can be applied to flat specimens. Both the vertical and the horizontal actuators can be either force or displacement controlled.

All experiments in this paper were carried out under constant crosshead velocity. When tightening the grips on specimens, a small amount of stress can be introduced due to the Poisson effect in the material between the grips. After the specimen is clamped into position the Instron can be temporarily switched to force control in order to zero the force before the test begins. This is a small detail but can greatly increase accuracy.

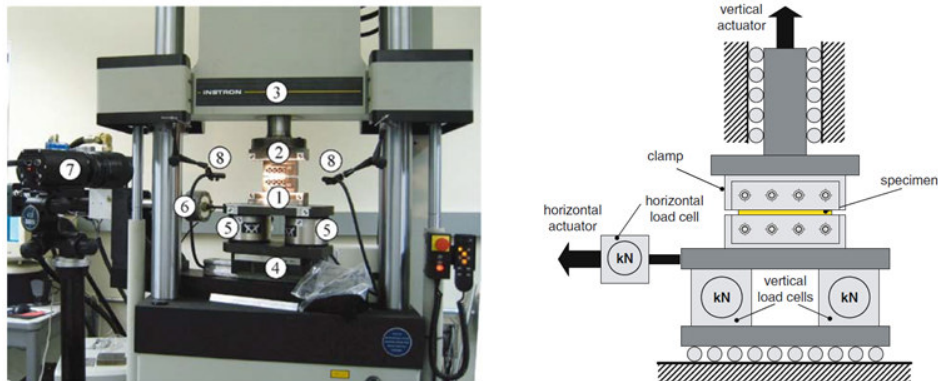


Figure 6: Dual actuator loading frame and system schematic, 1—lower specimen grip, 2—upper grip, 3—upper cross-head, 4—sliding table, 5—vertical load cells, 6—horizontal load cell and actuator, 7—digital camera (Mohr and Oswald 2008).

### 2.1.2 Digital Image Correlation (DIC)

Displacements and surface strain fields are measured using digital image correlation (DIC). The testing machines are displacement controlled and log a displacement output but for more accurate relative displacements the DIC software is used. The software analyses pictures taken at 1 second intervals during the experiment. The specimen being tested is painted with a thin layer of white paint which is then 'speckled' with black paint (Figure 8). The average speckle size is about 70  $\mu\text{m}$ . This speckling gives the camera reference points to follow during the analysis. Running the test shortly after the paint is applied helps to ensure the paint does not delaminate from the specimen surface. Before the test begins, through the completion of the test (specimen fracture) a high resolution digital camera is constantly taking still images of the specimen. The DIC software allows the user to select a reference picture which will be a still shot before the test begins. The rest of the pictures, in order, are selected as the deformed images. An area can be selected to obtain a contour plot of the surface strains, as seen in Figure 7.

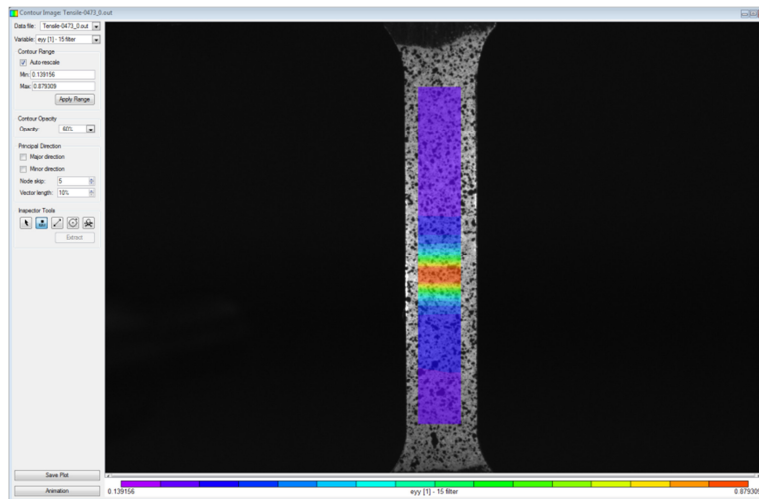
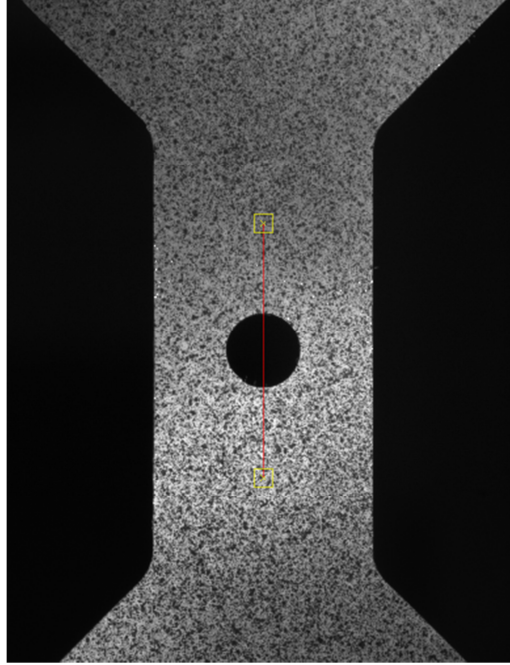


Figure 7: DIC strain contour plot.

The exact position of the emerging neck in uniaxial tension tests is unknown before the experiment. The contour plot helps show the strain evolution throughout the test and helps with placement of the virtual extensometer. Two points can be selected generating a virtual extensometer along a straight line. The software will track those points and give accurate relative displacements. Extensometers in a horizontal line on the reference image can be seen in Figure 8.



**Figure 8: Extensometer placement.**

By precisely placing these points the experimental displacement/strain data can be precisely matched to the numerical simulations (see section 3.3).

Force is output by the testing machine's sensors, displacement is measured using DIC, and stress/strain is calculated. The images captured as well as the forces logged are on a time basis and matched exactly. Large deformation theory is used due to the high levels of strain achieved. Substantial differences occur between engineering stress ( $\sigma_{eng}$ )/strain( $\varepsilon_{eng}$ ) and true stress( $\sigma_t$ )/strain( $\varepsilon_t$ ) at these high levels. Thus, true stress/strain is used throughout this study. Stress and strain is defined as

$$\sigma_{eng} = \frac{F}{A_0} \quad (1)$$

$$\sigma_t = \sigma_{eng}(1 + \varepsilon_{eng}) \quad (2)$$

$$\varepsilon_{eng} = \frac{\Delta L}{L_0} \quad (3)$$

$$\varepsilon_t = \ln(1 + \varepsilon_{eng}) \quad (4)$$

where  $F$  is the force applied,  $A_0$  is the surface area of the gage section of the specimen,  $\Delta L$  is the change in length of the extensimeter, and  $L_0$  is the initial length.

A special situation arises for the punch indentation testing. Due to the specimen geometry and out of plane deformations, 3-Dimensional (3D) vice 2-Dimensional (2D) DIC is required to get accurate displacement measurements. This involves the use of two cameras with different perspectives taking simultaneous images of the test specimen. The initial setup requires calibration so that one camera's position with respect to the specimen and the other camera is clear to the software. With images taken from both cameras a three dimensional view of the experiment can be seen by the software, giving extremely accurate displacement and strain data. Figure 9 shows the computer representation of the initial and deformed 3-D surface calculated for the punch indentation test.

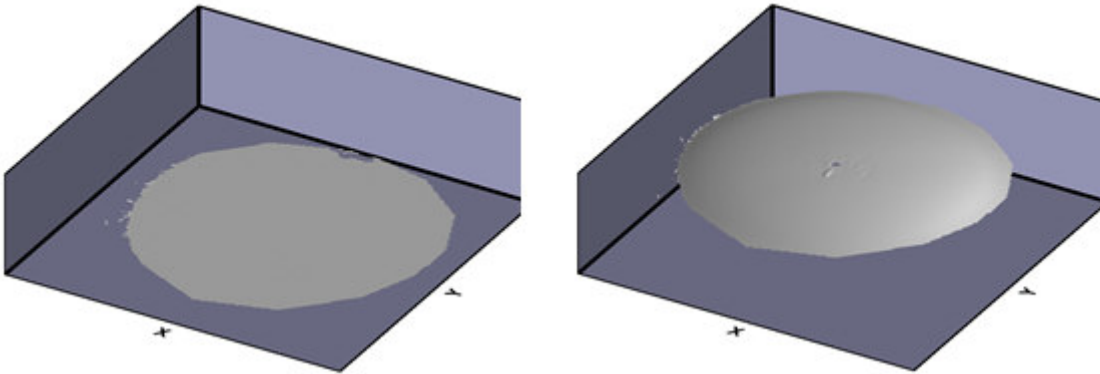


Figure 9: 3-D DIC surface representation of the initial and deformed surface.

## 2.2 Specimens

The steel used in the experiments was provided by NSWC Dahlgren. Due to its complex geometry and volatility to small manufacturing defects, the butterfly specimen was machined by the MIT machine shop (Figure 18). The other specimens were created in SolidWorks and cut using the OMAX water-jet (Figure 15 and Figure 16). The testing equipment used for the dog-bone specimens has micro and macro modes and can give more accurate results if the force sensors are kept below 10kN. For this reason, and to get a clean uniform surface the specimens were thinned to 1.5mm using surface grinding. All specimens, besides the butterfly specimens, were taken to 1.5mm to keep uniformity. During the grinding operation care was taken to not put too much heat into the material to prevent changing the material characteristics. The surface temperature rise during grinding is related to the process variables by the following expression (Kalpakjian and Schmid 2001):

$$\text{Temperature Rise} \propto D^{1/4} d^{3/4} \left( \frac{V}{v} \right)^{1/2} \quad (5)$$

$D$  is the diameter of the grinding wheel,  $d$  is the depth of cut (greatest influence on temperature),  $V$  is the wheel's tangential velocity and  $v$  is the work-piece velocity. The process is slow and coolant is constantly flowing over the work-piece.

## 2.2.1 Dog-bone Specimen

The dog-bone specimens are critical in defining the plasticity of the material. The specimen design is based on the ASTM standard (E8M) for tension testing metallic materials (Figure 10) with a nominal gage width of 6mm (ASTM 2001).

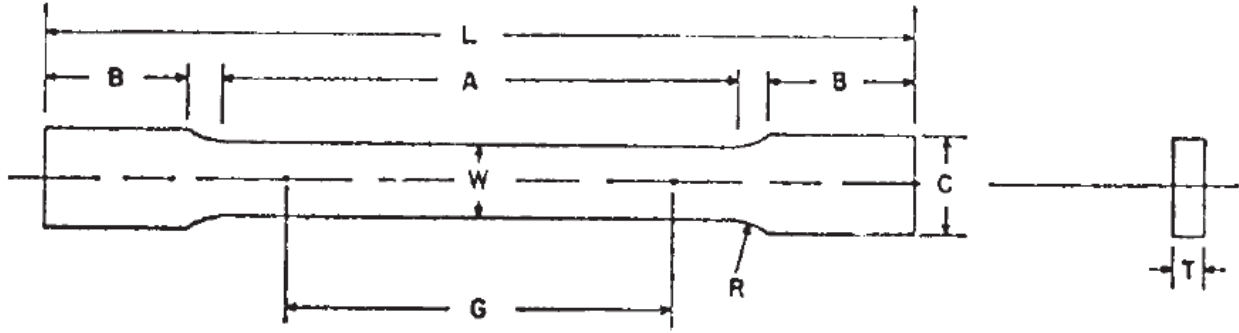


Figure 10: ASTM tensile dog-bone specimen (ASTM 2001).

The plasticity modeling follows the methods described in Dunard and Mohr (2010a) and Beese et al. (2010). Standard plasticity theory is used with an anisotropic quadratic Hill (1948) yield function, associated flow rule, and an isotropic hardening model. Isotropic hardening means the initial yield value may depend on material direction but the hardening curves will be parallel to each other. The assumption is confirmed by load-displacement curves that do not vary over the directions.

### 2.2.1.1 Hardening Rule

The strain-hardening behavior of the steel is determined from uni-axial tension tests on the dog-bone specimens. The tests establish the stress-strain curve which is needed as a material input to the FE simulations. The FE software takes plastic strain ( $\varepsilon_p$ ) as an input,

$$\varepsilon_p = \varepsilon_t - \varepsilon_e = \varepsilon_t - \frac{\sigma_t}{E} \quad (6)$$

where  $\varepsilon_e$  is the elastic strain and  $E$  is the Modulus of Elasticity. The maximum load in the experiment is reached just before the specimen develops a neck, due to strain localization. This is at a relatively low value of  $\varepsilon_p$ ; thus, a power law, or Swift law, is used to extrapolate the mechanical behavior at higher strain rates.

The power law used is

$$\sigma_t = A(\varepsilon_p + \varepsilon_0)^n \quad (7)$$

and the Hardening law would be represented by

$$H(\varepsilon_p) = An(\varepsilon_p + \varepsilon_0)^{n-1} \quad (8)$$

A and  $n$ , the two parameters of the power law, can easily be found by fitting a trend-line (Excel) using the method of least squares.  $\epsilon_0$  is the strain at initial yield. Figure 11 is a plot of the combined experimental data with the analytical power law extrapolation of true plastic stress at higher strains. This figure is revisited in Section 3.1 where the data is implemented into the FE software. The true necking strain  $\epsilon_n$  should equal the strain hardening exponent of the power law  $n$ .

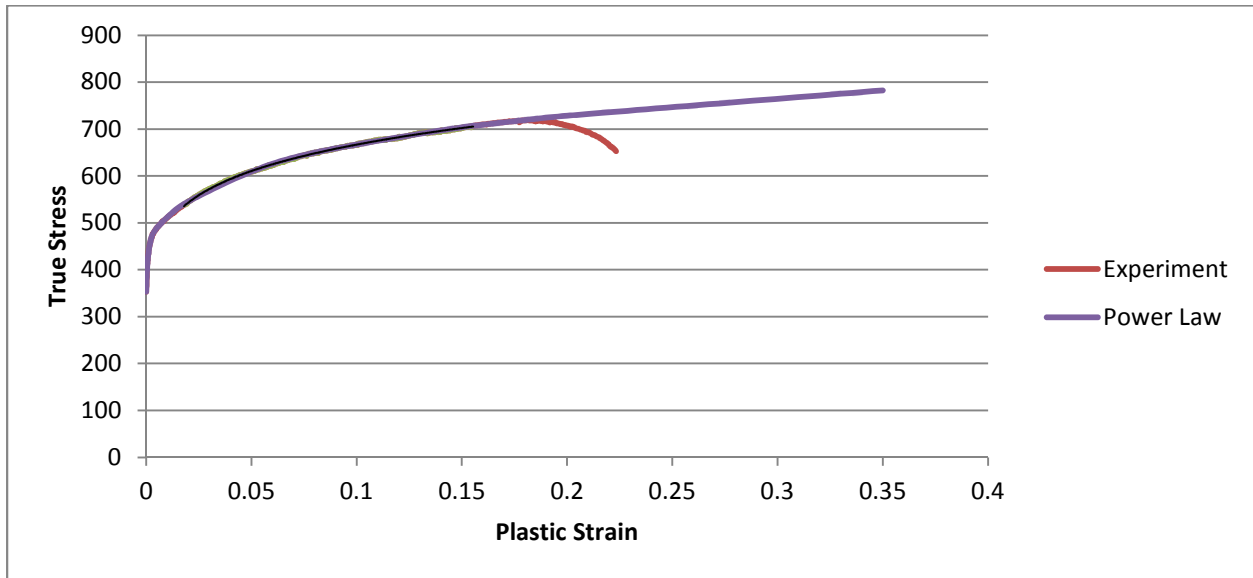


Figure 11: Power law extrapolation.

### 2.2.1.2 Anisotropy

Anisotropic materials have physical and/or mechanical properties that are directionally dependent. For rolled steel these properties typically correspond to the rolling direction. The microstructure of the material can change with the direction of the material as well as through the thickness. Nemat-Nasser and Guo tested DH-36 in the rolling direction as well as perpendicular to the rolling direction (2003). Their results showed that the mechanical properties did not depend on the orientation or the through thickness location of the samples. In the current study, in order to determine the degree of anisotropy in the material, dog-bone specimens were extracted at zero, forty five, and ninety degrees to the rolling direction, with zero defined as the rolling direction. Figure 12 illustrates the concept and also shows that planning and care needed to be taken during the water-jet operation to maximize the use of material. Three tests were conducted for each orientation.



**Figure 12: Dog-bone orientation with respect to the rolling direction.**

The measurement used to quantify the amount of anisotropy is the Lankford ratio ( $r_\alpha$ ), where  $\alpha$  is the angle measured from the rolling direction. The parameter is the ratio of the strain in the width direction to the strain in the through-thickness direction.

$$r_\alpha = \frac{d_{\alpha+\pi/2}}{d_{\varepsilon_3}} \quad (9)$$

DIC enables accurate measurement of in plane strains  $\varepsilon_x$  and  $\varepsilon_y$ . The plastic incompressibility condition is utilized to express  $\varepsilon_3$ , thickness reduction, as  $-(d_{\varepsilon_x} + d_{\varepsilon_y})$ . The Lankford parameter is important in drawing and stamping operations. A fully isotropic material will have a Lankford ratio equal to unity. If the ratio is greater than unity it is more difficult to reduce the thickness of the material than having it drawn from a blank. Figure 13 shows the relationship of transverse and through thickness strains for the specimens in all three directions. The slopes of the lines correspond to the  $r_\alpha$  values. As observed by Nemat-Nasser and Guo there is little to no anisotropy between the rolling direction ( $0^\circ$ ) and the transverse direction ( $90^\circ$ ).

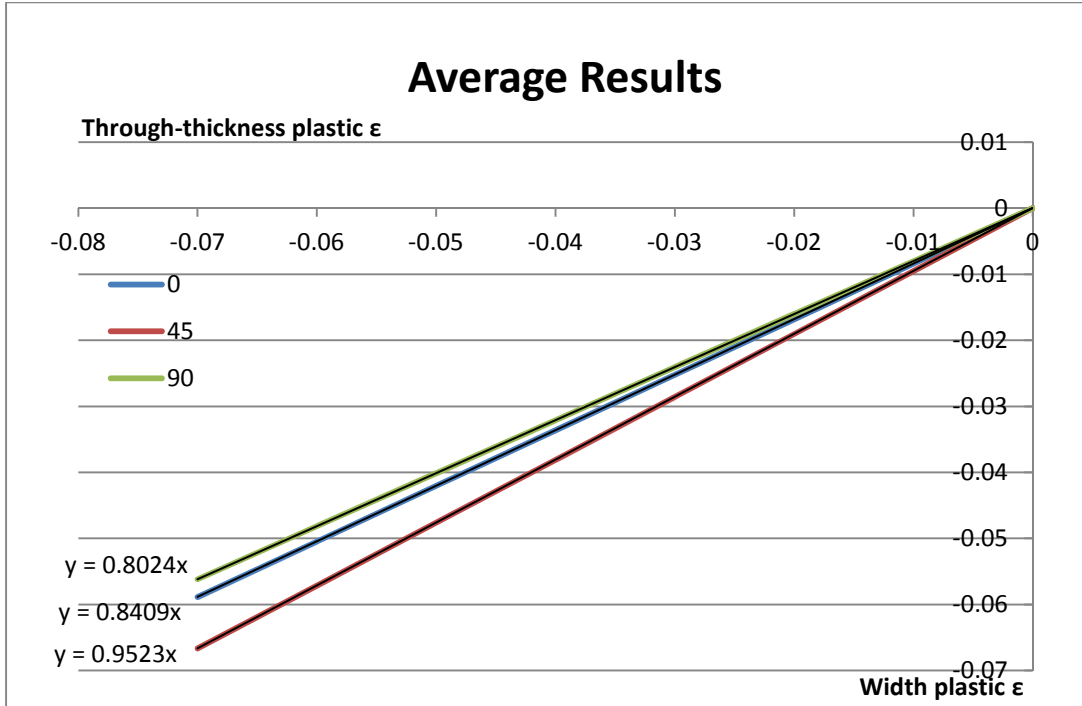


Figure 13: Average transverse (width) plastic strain versus through-thickness plastic strain for three specimens in each orientation.

There is very little through thickness anisotropy through the material, in that all tests are close to unity. However, there is slight anisotropy at the 45° direction. According to Mohr et al. (2010a)  $r_\alpha$  can be plotted as a function of  $\alpha$  from 0° to 90° knowing only the 0°, 45° and 90° directions, Figure 14.

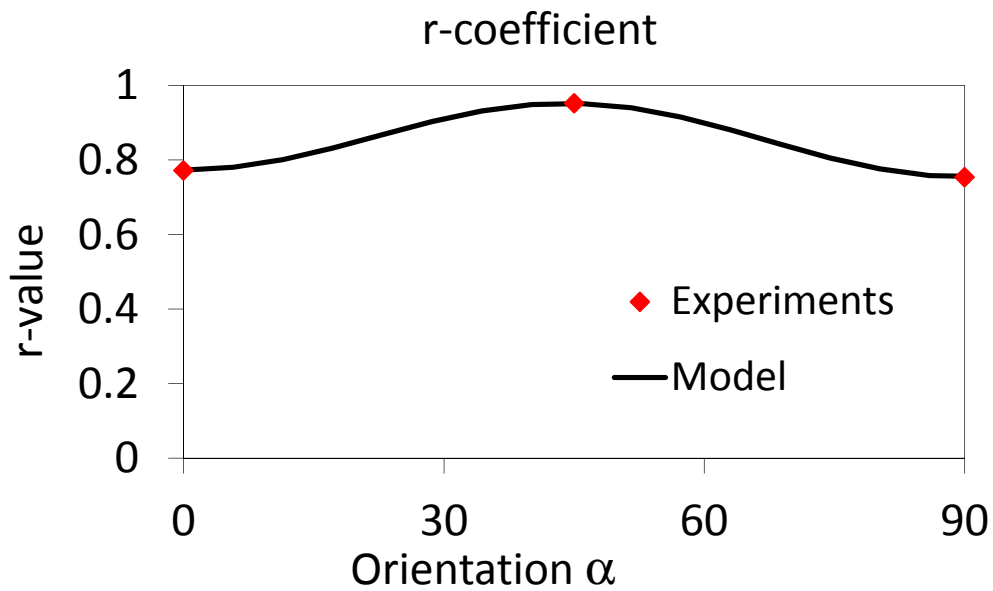


Figure 14: Lankford coefficient plot.

Abaqus, the FE software used in this project uses “anisotropic creep stress ratios”  $R_{ij}$ , which can be thought of as yield ratios to express/accept the Lankford data (Abaqus 2011).

$$R_{11} = 1 \quad (10)$$

$$R_{22} = \sqrt{\frac{r_y(r_x + 1)}{r_x(r_y + 1)}} \quad (11)$$

$$R_{33} = \sqrt{\frac{r_y(r_x + 1)}{(r_x + r_y)}} \quad (12)$$

$$R_{12} = \sqrt{\frac{3(r_x + 1)r_y}{(2r_{45} + 1)(r_x + r_y)}} \quad (13)$$

Without having data on the out of plane shear, it is assumed  $R_{13} = R_{23} = 1$  (isotropic). The anisotropic ratios and material orientation is assigned in abaqus when conducting the FE simulations. The anisotropy analysis defines the vertical axis of the specimen as ‘x’ and the horizontal axis as ‘y’, a 90° rotation about the z axis.

### 2.2.2 Notched and Hole Specimens

A variety of specimens, other than the dog-bone specimens, are used to characterize the dependence of the fracture locus on the type of loading and state of stress. The fracture locus is a three-dimensional (3D) surface. The specimens are designed to give data points over a broad range of the stress parameters  $\eta$  and  $\bar{\theta}$ , so an accurate interpolation can be carried out.

The first type of specimen to be considered is the tensile specimen with a central hole. The dog-bone is a standard uni-axial tension test specimen. It is not used for fracture surface calibration because the stress state varies throughout the experiment from uni-axial tension to transverse plane strain. This variation is due to the significant neck that develops at large strains. In order to mitigate this variation throughout the experiment and keep a more constant stress state, specifically triaxiality, the tensile specimen with a central hole is used (Figure 15). This feature forces the fracture to initiate at the

intersection of the hole and the transverse axis of symmetry of the specimen.

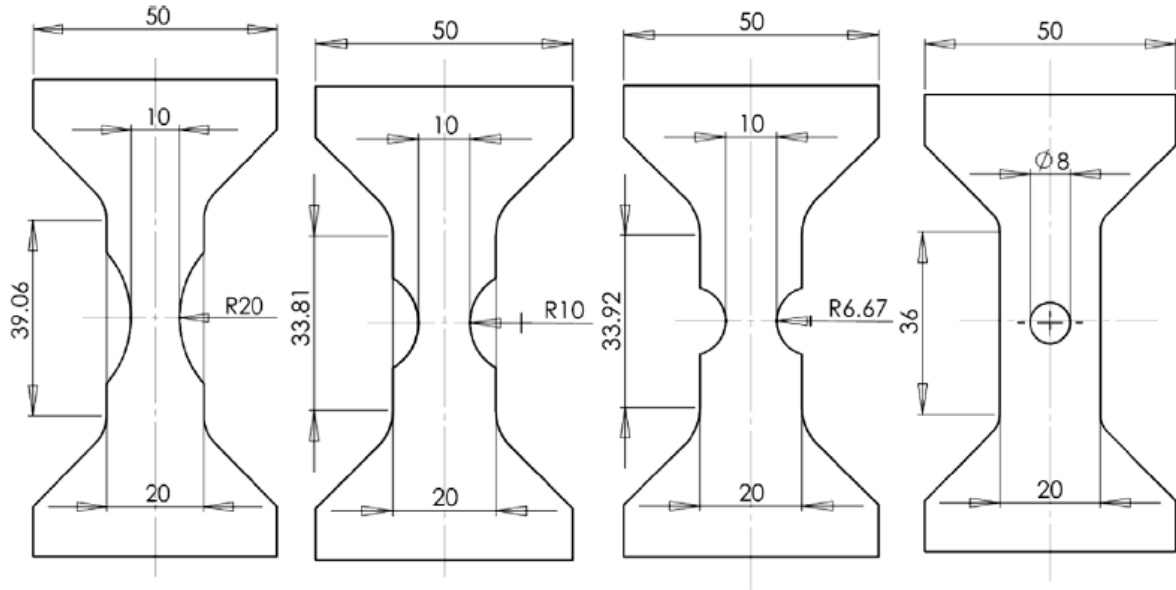


Figure 15: Tensile specimens with different notch radii and a central hole (Dunard and Mohr 2010a).

Testing is also carried out on similar geometries, the notched specimens. These are flat tensile specimens with circular cutouts (Figure 15). The triaxiality within the specimen is a function of the notch radius, thus a range of stress states can be achieved. The expression for initial triaxiality is given by:

$$\eta = \frac{1 + 2\Lambda}{3\sqrt{\Lambda^2 + \Lambda + 1}} \quad (14)$$

where  $\Lambda = \ln[1 + t/(4R)]$  and  $R$  denotes the radius of the cutout (Y. Bai 2008). The stress state approaches uni-axial tension (dog-bone  $\eta = 0.333$ ) as the notch radius increases. It approaches plane strain ( $\eta = 0.577$ ), along the width of the specimen, as the notch radius decreases. Three different notch radii are used,  $R = 20\text{mm}$ ,  $R = 10\text{mm}$  and  $R = 6.67\text{mm}$ . The central hole and notched specimen loading axis is always oriented along the rolling direction.

### 2.2.3 Punch Specimen

The punch tests performed demonstrate fracture under an equi-biaxial state of stress. The geometry can be seen in Figure 16. The outer holes are for bolts used to clamp the outside of the specimen into a specially designed die.

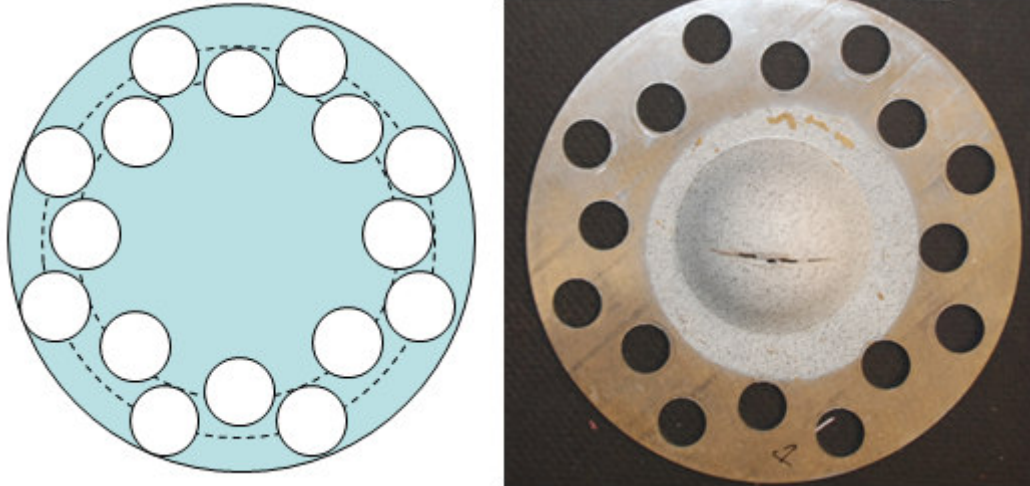


Figure 16: Punch specimen schematic and post test.

The tests were performed in the MTS loading machine. Sandwiched sheets of Teflon (5 at .002 in-thick) and grease were used in between the hemispherical punch and specimen to eliminate unwanted frictional forces that would disturb results. The apex of the dome created during the test (Figure 16) is the most highly-stressed point where radial and circumferential stress and strain are equal to each other.

#### 2.2.4 Butterfly Specimen

The butterfly specimen is designed to maintain uniform stress and strain fields during combinations of normal and tangential loading. Mohr and Oswald outlined the details of the multi-axial testing procedure (2007).

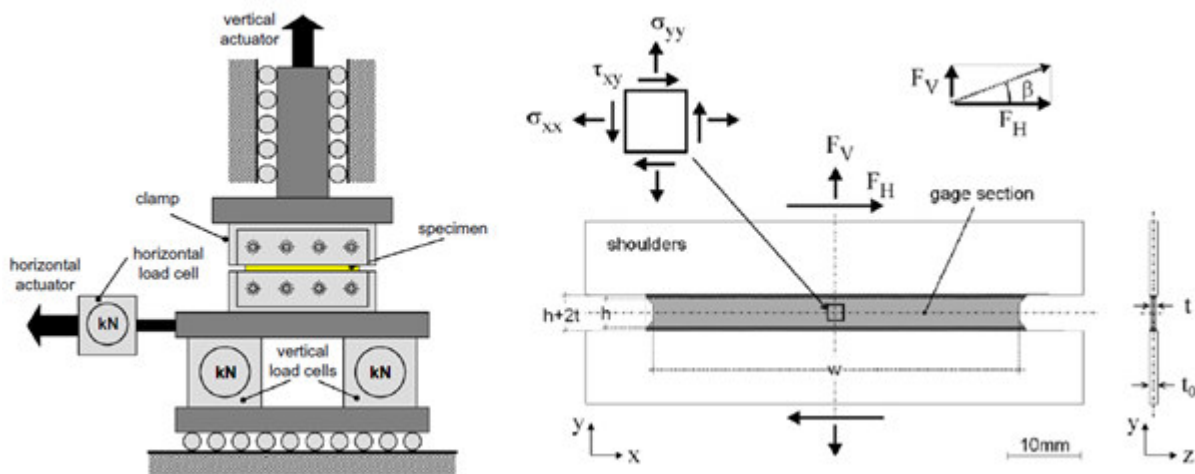


Figure 17: Dual Actuator Loading Frame and definition of the bi-axial loading angle  $\beta$  (Mohr, Dunard and Kim 2010).

Figure 17 demonstrates the bi-axial loading angle  $\beta$ . In the current calibration, tests were only conducted at the limiting cases of  $\beta = 0^\circ$  and  $\beta = 90^\circ$  corresponding to pure shear and transverse plane strain respectively. The specimen geometry has changed over the years but was recently optimized by Dunard and Mohr and can be seen in Figure 18 (2009). The geometry is optimized to ensure fracture initiates remote from the free specimen boundaries regardless of loading angle. The design prevents unwanted plastic deformation, high strain concentrations, crack initiation and/or buckling. It also fulfills the obvious task of fitting the dual actuator loading frame and meeting manufacturing constraints.

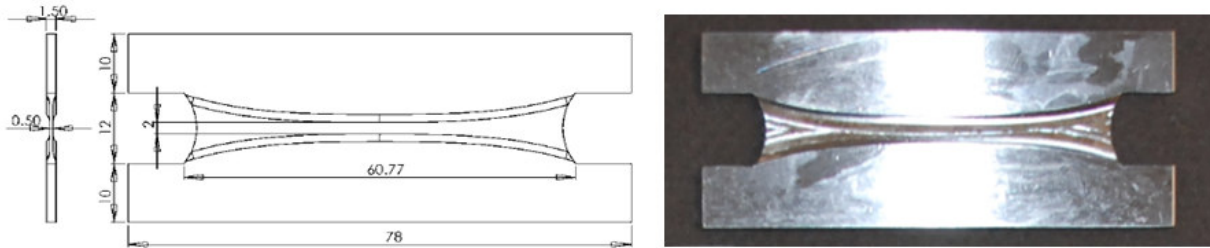


Figure 18: Optimized butterfly specimen (Dunard and Mohr 2009).

Fracture initiates at the center of the specimen and the crack propagates in a stable way toward the boundaries in a kinematically-controlled test. During pure shear testing, the horizontal actuator is in displacement control and the vertical actuator is in force control, maintaining a normal force of zero. Selected images from experimental testing are included in Appendix B.

### 3 Numerical Simulation

#### 3.1 Hybrid Approach

There are two main reasons numerical simulations are necessary. First, the material points where fracture initiates are inside the specimens. It is impractical to attempt to make observations and retrieve data from the center of a specimen in a physical test. Also, the data and parameters required from the tests, even if fracture were to occur on the surface, are extremely complicated and can be calculated quickly and accurately using FE software. The simulations provide perspective on the evolution of the third invariant, von Mises stress, pressure, triaxiality and equivalent plastic strain up to fracture initiation. The hybrid-approach used is based on the work of Dunard and Mohr (2010a).

#### 3.2 Setup

Implicit finite element simulations were conducted using Abaqus/standard. The notched and central-hole specimens were meshed using reduced-integration eight-node 3D solid elements (C3D8R in the Abaqus library). In order to save on computing time, the simulations took advantage of the symmetry of the specimen's geometry, material properties, and loading conditions. Thus, only one eighth of the specimen, half the thickness of an upper corner, was modeled. X, Y, and Z symmetry planes were assigned.

Mesh size (mesh density) has a tremendous influence on FE simulation results. A ‘fine’ mesh, as described by Dunard and Mohr, was used to provide a good balance of computational time and efficiency (2010a). They define this mesh as having a minimum size of 0.1mm per element and 8 elements through the thickness (.75mm model / 1.5mm specimen the same as this study). Their analysis showed that doubling the mesh size from fine to very fine would only contribute to an output variation of 0.2%. In the 6.67mm notched specimen the model was partitioned in the area of the localized neck to assist in convergence of the results (Figure 21). The simulations were run with 100 implicit time steps, which will also give less than .2% variation in final plastic strain. The butterfly tension test was also given a fine mesh. Y and Z symmetry were assigned to a point on the top of the specimen. YA symmetry (anti-symmetry) was assigned to the bottom face and the bottom face was selected for displacement. The grip sections were not modeled in order to save computing time (Figure 19). More simulation results can be seen in Appendix B.

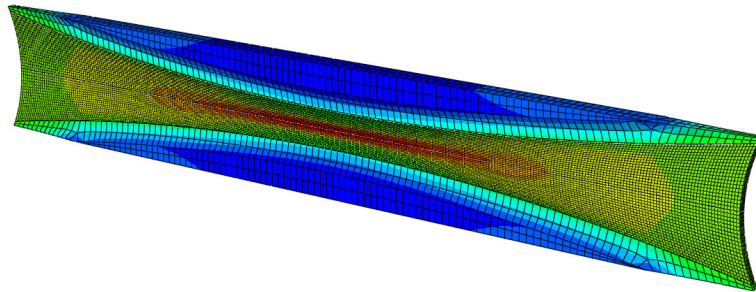


**Figure 19: Butterfly specimen in tension with a von Mises stress contour plot.**

The punch and butterfly shear tests were modeled using reduced integration S4R shell elements. The punch itself was modeled (constrained) as a rigid body with a frictionless surface-surface interaction imposed. A quarter of the punch specimen was modeled, again to take advantage of symmetry. The edges corresponding to planes of symmetry were restricted to zero normal displacement or edge rotation (symmetry boundary). The outer edge, which corresponds to the clamped section, was modeled as fully clamped (encastre) (Figure 20).

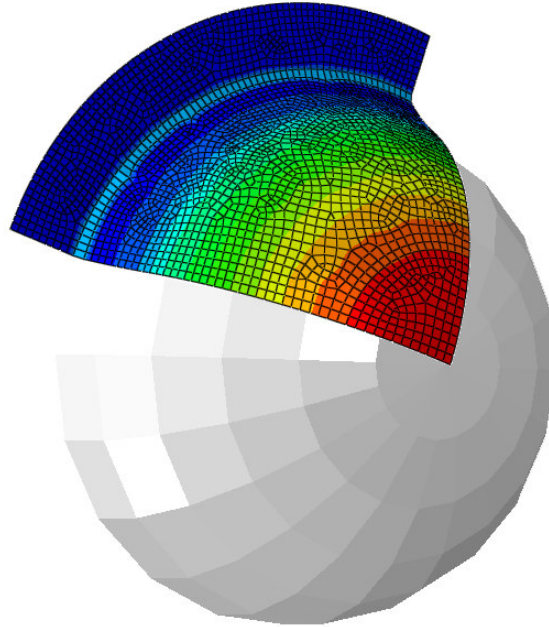


**Figure 20: Punch test simulation with equivalent plastic strain (PEEQ in Abaqus) contour plot.**

The full butterfly in shear specimen was modeled. A point on the bottom of the model was given X and Z symmetry. The top surface is given XA symmetry and moved in displacement.

Material properties are one of the most important inputs for the simulations. The elastic material behavior is input as the Young's Modulus (E) and Poisson's ratio ( $\nu$ ). The anisotropic potential is entered using the anisotropic ratios  $R_{ij}$  described in section 2.2.1.2. Finally, the plastic material behavior is entered as points on the plastic strain vs. stress curve. The plastic behavior is important because it is what is adjusted to ensure the simulation matches the experimental results, validating the model.

### 3.3 Validation

In order to know the model is accurate it must be validated with the experimental data. The validation is completed by comparing and matching the force displacement curves of simulations and experiments. The stiffness of the testing devices can interfere with the measured displacements from the testing machines themselves. An example of that would be strain in the loading frame. Therefore, DIC is used, which takes displacement measurements directly from the surface of the specimen. The specimen geometry in the simulation is designed to have the same boundaries as the extensometers in the physical tests, as seen in Figure 21.  $2h$  is the extensometer distance,  $h$  is taken as the 1/8th model height in the simulation,  $\Delta u$  is the displacement in the test and  $\Delta u/2$  (in the case of 1/8 and 1/4 models) is the displacement in the simulation. This modeling method was used for all notched, hole and butterfly tests.

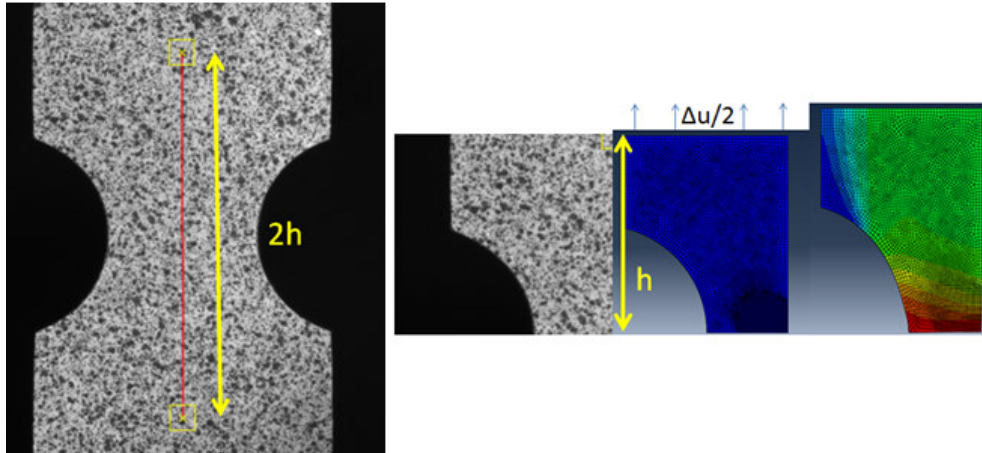


Figure 21: Extensometer placement and matched FE model for the 6.67 notched specimen.

As mentioned above, to accurately match the simulation to the experiments, the plastic behavior of the material entered into the software is adjusted. The adjustments are methodical in order to save time and get the most accurate results. To start, the number of points on the plastic stress vs. strain curve entered into the software can affect the output. A good rule of thumb for selecting data points on the stress strain curve is to use a strain increment of .01 up to the necking point, then select strain increments of .1 from there on. This spacing of entry points can be seen in Figure 22, where the purple x's mark the points entered into the FE software. The stress values, until the neck is formed, are taken from the experimental measurements. After the neck is formed the extrapolated power law values are used. The power law is derived using the experimental data from the yield point up to the neck.

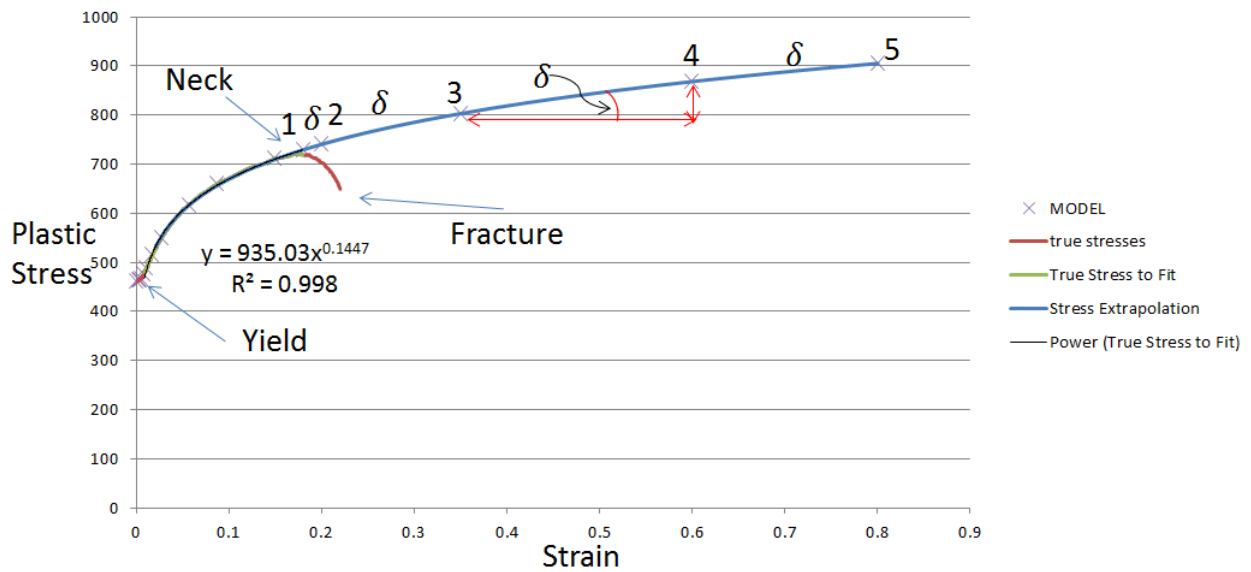


Figure 22: Material plastic behavior.

The adjustment, in order to match simulation to experiment, takes place between the points labeled 1 thru 5. The slopes ( $\delta$ ) between the points are calculated. These  $\delta$ 's are then used as 'triggers' to adjust the plastic stress up or down. The force displacement curve from the simulation is compared to that of the actual experiment. If the force in the simulation is too low the plastic stress is slightly increased by these triggers and the simulation is re-executed. The process repeats until the force displacement curves match. The outcome is shown using Figure 23. The plot shows, for the central-hole tests, the two experimental force displacement curves as well as the ensuing simulations until a match was reached. In this case, 9 iterations were needed. Also, the 6.67 notch test and simulation curve are shown in Figure 24 to give a clear view of the match. All simulations need to be matched in this way to ensure accurate data is coming from the simulation. More plots are included in Appendix B.

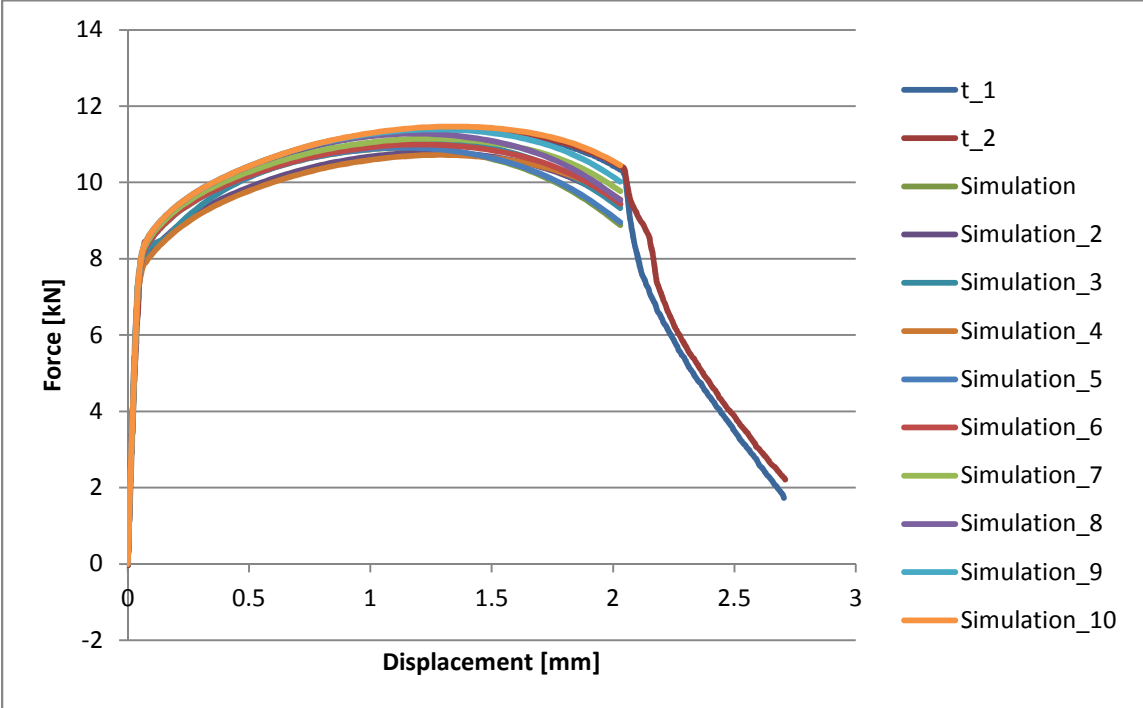


Figure 23: Force displacement simulation test series for the central hole specimen.

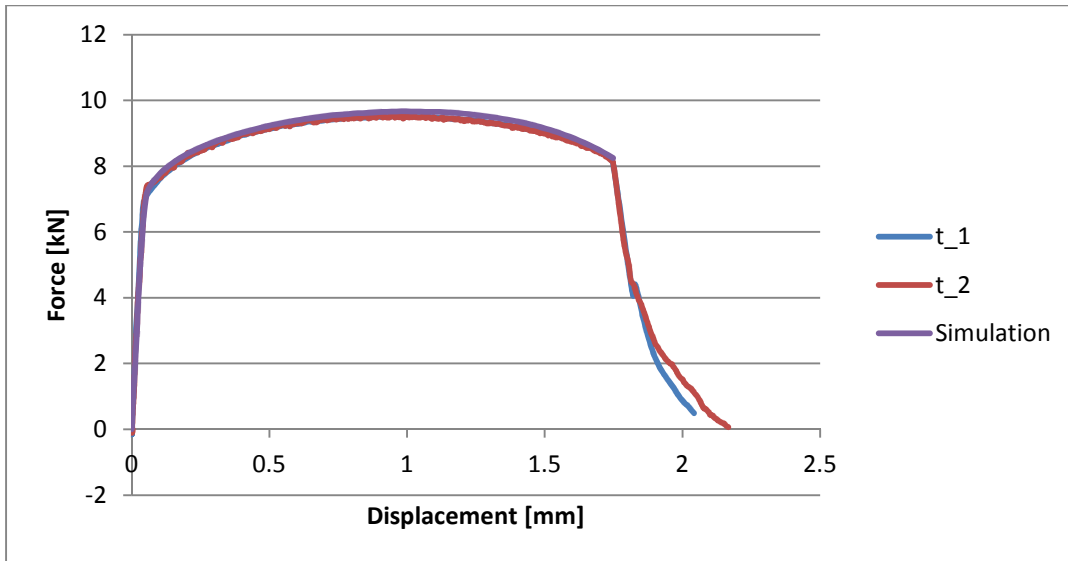


Figure 24: Force displacement simulation comparison for the 6.67 notched specimen.

The punch test is a special case. Due to the geometry and the out of plane deformations 3-D vice 2-D DIC is required (section 2.1.2). For the two cameras to capture images during the test an angled mirror is placed under the specimen and its clamping frame. The cameras can then be directed at this mirror giving them a view of the underside of the test. Figure 25 shows the 3-D DIC displacement contour plot at a time close to fracture. Displacements shown are in the direction of the punch's path. This is an image from one of the two cameras used during the test. The circles appear to be off centered because the camera is not perfectly centered on the specimen. It is not centered because the cameras need different perspectives of the specimen to capture the relative displacement and thus the third dimension, they are not perfectly centered on the test area. Using the software, points on the image can be selected, and displacements or strains can be extracted for that point over the duration of the test.

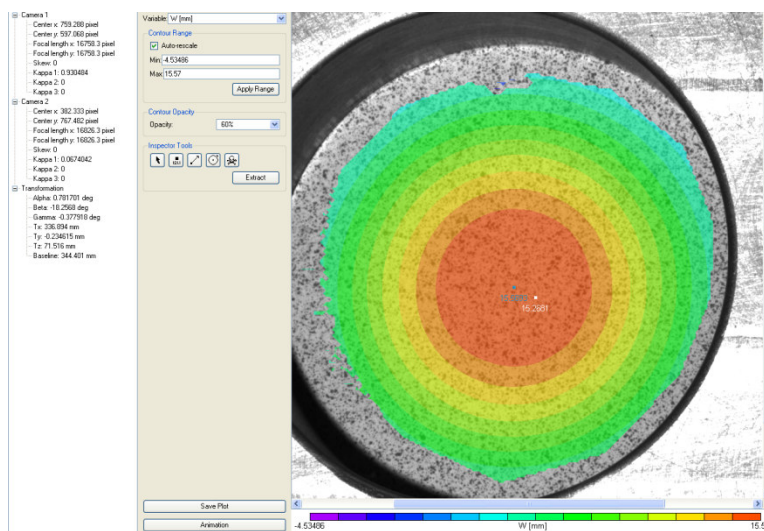


Figure 25: 3-D DIC displacement contour plot.

Two punch tests were executed. In the second test, due to the high ductility of the material, the painted speckle pattern de-laminated from the specimen surface before fracture, which restricted the use of DIC in that test. The degraded paint near the fracture point can be seen in Figure 26.

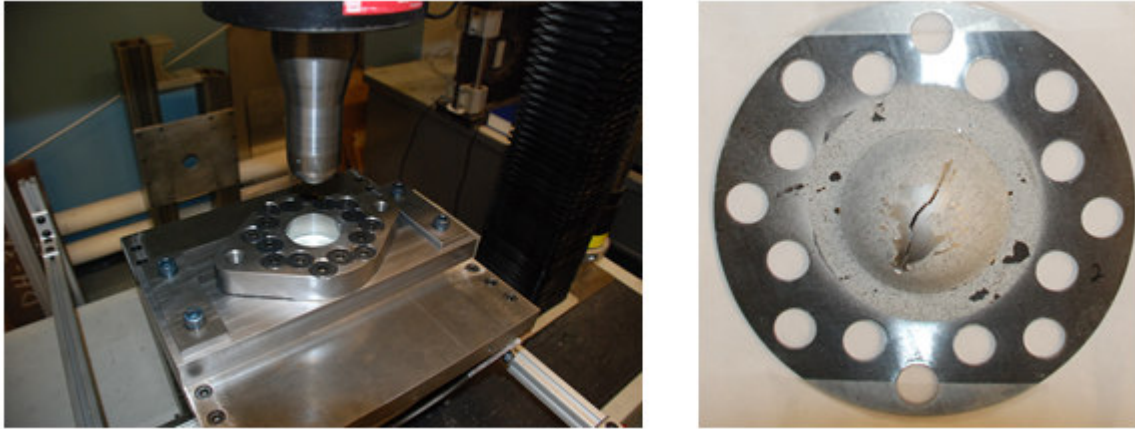


Figure 26: Punch test setup and specimen after fracture.

As stated above, displacement measurements can be taken from the MTS loading frame instead of using DIC. However, that data is affected by the behavior of all the devices located between the specimen and the measurement device. Since DIC data for the second punch test could not be obtained, the force displacement curve with MTS displacement data was taken and compared for the first and second test, simply to confirm repeatability. The punch test is a very repeatable test, which is confirmed in Figure 27 by the series 'Test\_1' and 'Test\_2'. Also shown in the figure, the FE simulation was matched to the 3-D DIC plot for the first test, showing a good match. Notice the simulation goes past the actual fracture displacement. This overshoot is not incorrect and is discussed further in section 3.4

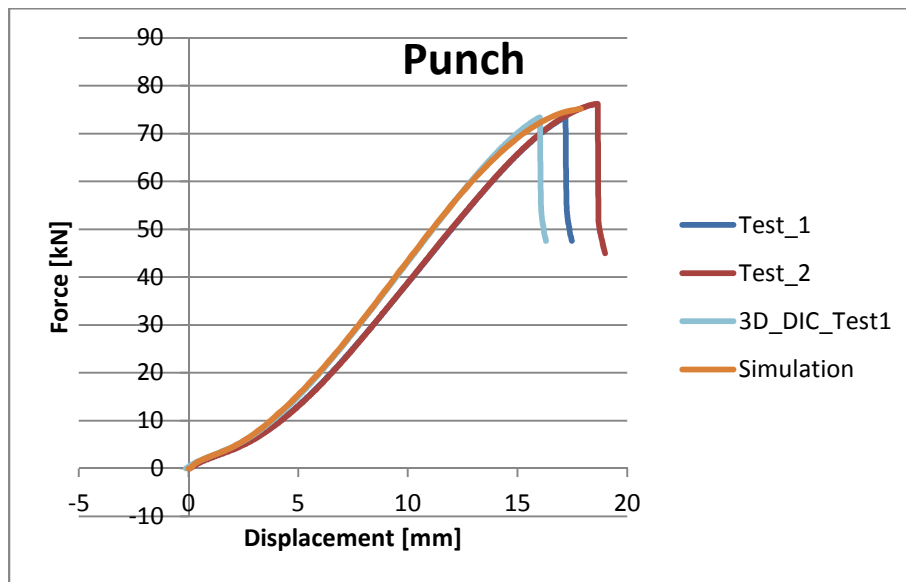


Figure 27: Punch force displacement curve.

### 3.4 Data Analysis

Once the simulations are validated the history responses of the pertinent parameters can be easily extracted from the FE software. All stages of the experiment are captured in the simulations including elastic deformation, yield, plastic deformation, diffuse necking, onset of fracture, and final fracture (rupture). This evolution can be seen in the experimental stress strain curve of a dog-bone specimen (Figure 28).

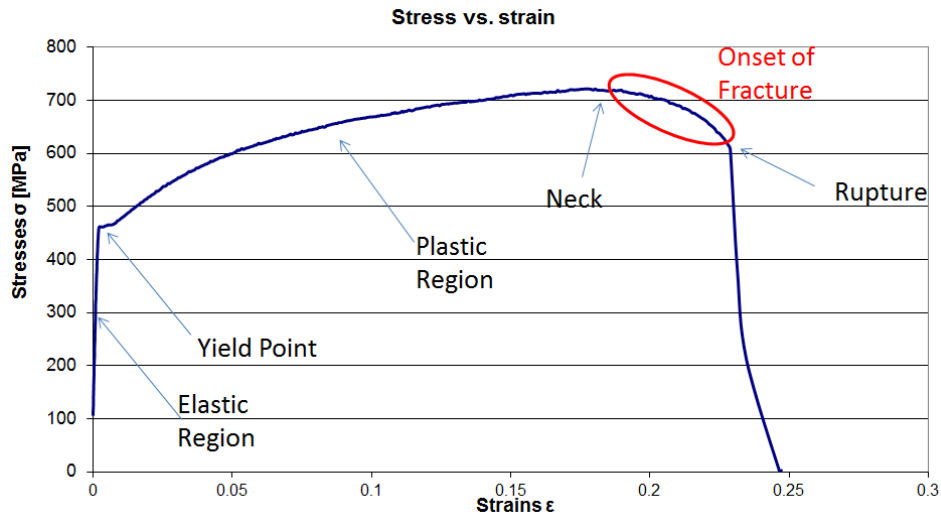
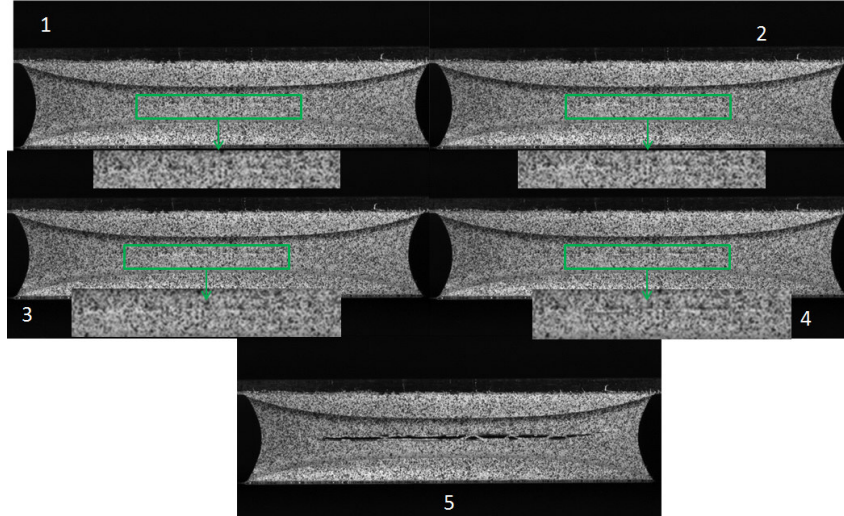


Figure 28: Typical stress strain curve.

The values that describe the state of stress and equivalent plastic strain are changing throughout the experiment and simulation. The final values used in the fracture model are not the numbers at final rupture. If they were, the process of pulling the correct data from the simulation would be much easier, in that the displacement at rupture could just be read at the start of the steep drop in the stress strain plot. The actual fracture initiation is located somewhere between neck formation and rupture, the red circle in Figure 28. The process for finding this point involves going back to the images, taken for DIC, and finding the point in time where the first surface discontinuity occurs. The corresponding displacement in the given test will give the exact point in the simulation where the stress states for calibration are taken. Figure 29 shows the transition and identification of onset of fracture for the butterfly specimen in tension. The identification of onset to fracture is crucial because plastic strain can change, especially in a ductile material, on the order of 10%. The images labeled 1 to 4 are the first four images, taken over 4 seconds, where onset of fracture is observed. A zoomed in image of the fracture area is included. The sub-figure labeled 5 is taken later in time when fracture is much more evident.



**Figure 29: Fracture evolution in the butterfly specimen in tension. 1-4 show the first four seconds of onset of fracture with a zoomed in image. 5 is taken at a later time to show a clear fracture.**

The determination of the onset of fracture in the shear test was supposed to be an easy task but in fact turned out to be difficult. Ideally, the butterfly specimens are not supposed to buckle at the edges. However, this material is extremely ductile so some buckling was observed prior to the onset of fracture. Figure 30 gives a front and back view of a butterfly specimen after shear testing. Buckling changes the stress state in the specimen. Even though there was buckling, the experiments were run until fracture occurred. It occurred at the edges of the specimen, not in the middle as designed. The FE simulation shows the maximum equivalent plastic strain occurs at the center, not the edges. If the MMC fracture model is correct it should predict fracture in the area where equivalent plastic strain is the largest. The discrepancy between the experimental observation and FE simulation is attributed to the so called edge effect. On the edge, small and sometimes invisible micro-cracks/imperfections caused by the manufacturing process reduce material ductility initiating fracture. The decision was made to take the data for calibration at the point with the maximum equivalent plastic strain in the center of the specimen. The moment the edge fracture occurred was taken as the displacement to fracture. This decision is a cautious engineering estimate. The green boxes are the areas of focus and the red lines highlight the unwanted buckling and fracture.

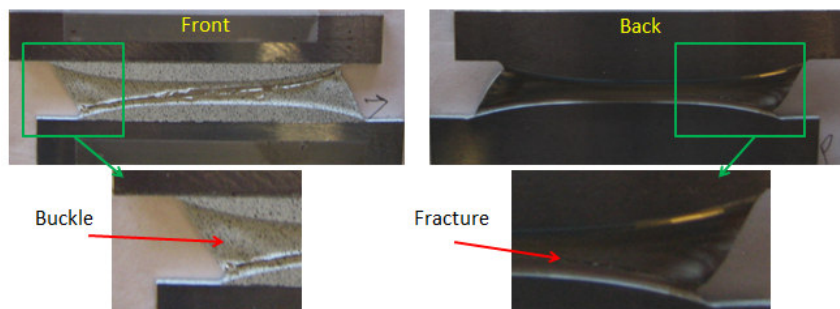


**Figure 30: Butterfly shear test showing front and back views and highlighting the unwanted edge buckling and fracture.**

### 3.5 New Shear Specimen

Due to the problems experienced with the butterfly specimen used for shear testing, a new type of specimen was examined to achieve pure shear all the way up to the onset of fracture. The new specimen can be seen in Figure 31.

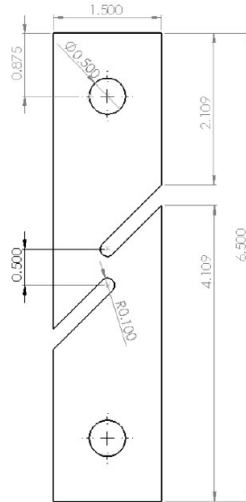


Figure 31: New Shear Specimen (inches).

The specimen is commonly used in industry and is meant to more easily achieve shear by utilizing a simple geometry which can be tested on a standard loading frame. It is worth noting the measurements shown are in inches and the specimen was created with a thickness of 1.5mm, in order to be consistent with the other specimens in this analysis. The test was conducted using the MTS loading frame. The holes shown on the drawing were not machined because grips are used as the mounting apparatus on the MTS. In future testing a slightly wider grip section should be designed into the specimen (as seen in Figure 15) to mitigate any unwanted stress states near the grips; although, in the 2-D DIC analysis of the test there were not errant strains observed near the grips, so this test was still valid.

The experiments and data analysis were successfully conducted with very repeatable results. One observation is that the specimen needs to be mounted perfectly, aligned in exact symmetry, specifically in the vertical direction. Any misalignment will cause the specimen to take on a twisting action negating the desired pure shear scenario and putting the gage section into tension and/or torsion and thus creating an unwanted stress state and neck.

The finite element simulations had great correlation with the experimental force displacement curve. However, the specimen fractured at a much lower triaxiality and Lode angle than the safe estimate taken from the butterfly specimen simulations. This discrepancy is discussed further in section 4.2 and resulted in this new specimen's data not being used in the MMC model calibration

## 4 Modified Mohr-Coulomb Fracture Criterion

### 4.1 Data Collection and Calibration

With simulations complete the next step in the process is to determine the equivalent plastic strain as a function of triaxiality and Lode angle at the onset of fracture for all the specimens (more background is included in Appendix A). The equivalent plastic strain ( $\bar{\epsilon}_{pl}$  or PEEQ in Abaqus) at the onset of fracture is simply known as the fracture strain ( $\epsilon_f$ ). The equivalent plastic strain, third invariant, von Mises stress, and pressure can all be defined as history outputs and taken directly from the simulation results. Stress triaxiality and Lode angle are calculated from these outputs. Stress triaxiality, also known as the dimensionless hydrostatic pressure, is the ratio of the mean stress ( $\sigma_m$ ) to the equivalent stress ( $\bar{\sigma}$ ). It is the normalized pressure and gives the average level of stress and its distribution along all principal directions.

$$\eta = \sigma_m / \bar{\sigma} = -p/q \quad (15)$$

The mean stress can be written as the negative pressure (-p) and the equivalent stress can be written as the von Mises stress (q).

$$p = \sigma_{ii} = tr(\underline{\underline{\sigma}}) \quad (16)$$

$$q = \sqrt{\frac{3}{2}(\underline{\underline{S}}:\underline{\underline{S}})} \quad (17)$$

S is the deviatoric stress. The dimensionless Lode angle parameter is defined by  $\bar{\theta} = 1 - 6\theta/\pi$  so that  $-1 < \bar{\theta} < 1$ , where  $\cos(3\theta) = (J_3/\bar{\sigma})^3$  with  $\theta$  being the Lode angle. Sometimes the symbol  $\xi$  is used to represent the normalized third invariant.

$$\xi = (J_3/\bar{\sigma})^3 = (r/q)^3 \quad (18)$$

r and  $J_3$  both represent the third invariant of the stress deviator tensor. The dimensionless (normalized) Lode angle is used in the model and is solved for in the form:

$$\bar{\theta} = 1 - \frac{2}{\pi} \arccos(\xi) \quad (19)$$

All simulations were run until the complete failure (rupture) of the specimen. Each series of images for a given experiment is analyzed to find the image corresponding to the onset of fracture. From the image numbering in the DIC software the exact displacement at fracture initiation is interpreted. In the FE simulation, the element with the maximum equivalent plastic strain at the onset

of fracture is detected and recorded. This element is where the data describing the state of stress and strain is taken. Equivalent plastic strain is plot against Lode angle and triaxiality. The equivalent plastic strain vs. triaxiality can be seen in Figure 32 and the equivalent plastic strain vs. Lode angle can be seen in Figure 33. The new shear specimen (Section 3.5) was not used in the final calibration.

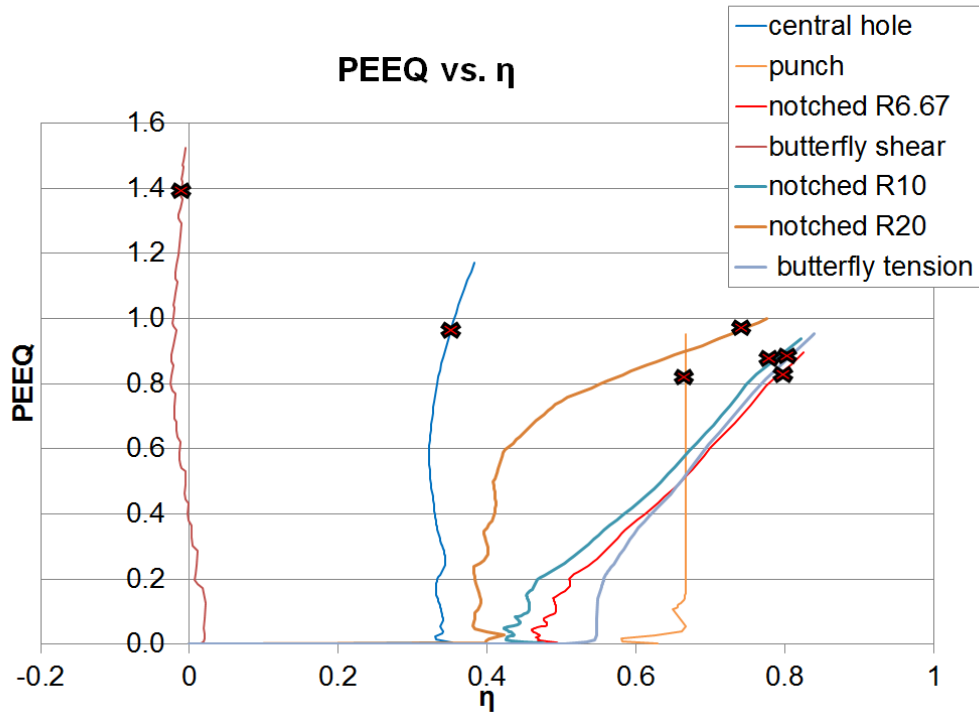


Figure 32: Equivalent plastic strain and triaxiality.

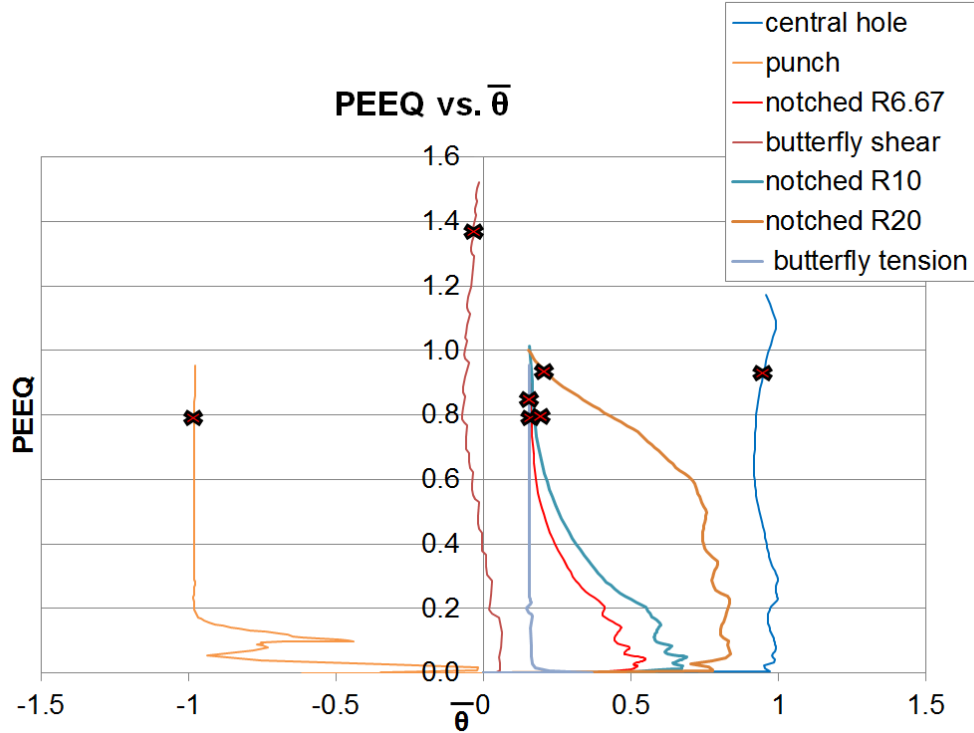


Figure 33: Equivalent plastic strain and Lode angle.

The displacement at onset of fracture is then used with the FE data to identify the onset of fracture on the plots, the red “x” shows where the onset of fracture occurred. The data is organized as seen in Table 1. Two tests were executed for each specimen but only one value of strain is given in the table. Only one value of  $\varepsilon_f$  is shown in the table because the displacement to fracture varied by less than one percent between similar specimens. Thus, the tests were very repeatable. The lower displacement value, vice an average, was used to obtain the fracture strain from the simulations. The displacement to fracture of the punch specimen varied by about 6 percent but only one of the experiments had useable 3-D DIC data, as discussed in section 3.3.

Table 1: Parameters used in model calibration.

| Table of Parameters |                |                 |  |                   |
|---------------------|----------------|-----------------|--|-------------------|
| $\eta$              | $\bar{\theta}$ | $\varepsilon_f$ |  | Specimen          |
| 0.775               | 0.164          | 0.793           |  | notched 6.67      |
| 0.762               | 0.169          | 0.829           |  | notched 10        |
| 0.732               | 0.185          | 0.839           |  | notched 20        |
| 0.349               | 0.953          | 0.925           |  | central hole      |
| -0.010              | -0.028         | 1.368           |  | butterfly shear   |
| 0.794               | 0.155          | 0.857           |  | butterfly tension |
| 0.667               | -0.979         | 0.805           |  | punch             |

## 4.2 New Shear Specimen Discussion

As stated in section 3.5 the new shear specimen experiment had very repeatable results. Also, the force displacement curve of the experiment and simulation showed good correlation; however, the specimen fractured at a much lower triaxiality and Lode angle then the safe estimate taken from the butterfly specimen simulations, even though the stress states should have been similar.

When looking at the simulation results, in the gage section of the specimen the triaxiality and Lode angle were similar to those of the butterfly specimen in shear. Thus, the gage section was in pure shear. The problem is that during the tests sharp edges form outside of the gage section, this can be seen in Figure 34 which shows the specimen prior to testing, half way through the test, one second before fracture, and one second after fracture.

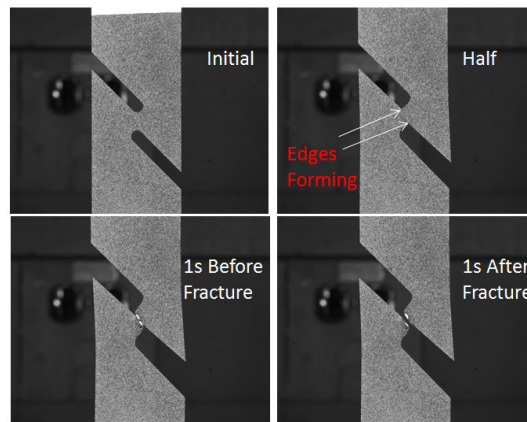


Figure 34: New shear specimen experiment prior to testing, mid-test 'half', one second prior to fracture, and one second after fracture.

It is difficult to tell for sure from the experimental data but it is possible that fracture initiates at these edges, which would make the test invalid. Ideally, fracture would initiate at the center of the gage section where the desired pure shear stress state is achieved. The FE simulations give more evidence to believe that fracture initiates outside of the gage section. In the simulation, at the displacement of failure the highest equivalent plastic strain is observed at one of these edges (Figure 35).

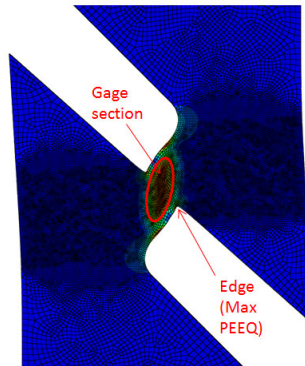


Figure 35: FE simulation PEEQ contour plot at the displacement of fracture, showing the maximum point of equivalent plastic strain in the edge section not the gage section. The face shown is the middle of the specimen.

Figure 36 shows equivalent plastic strain to fracture as a function of triaxiality and Lode angle. The new shear specimen's history is shown at the point in the gage section with the highest equivalent plastic strain (labeled 'new shear gage') and the point at the edge (labeled 'new shear edge') with the highest overall equivalent plastic strain in the specimen. From the plots it becomes clear that fracture in the new shear specimen seems to initiate early when looking at the gage section history. However, when looking at the edge, it fails as predicted from different specimens. These results led to the new shear specimen not being used in the calibration.

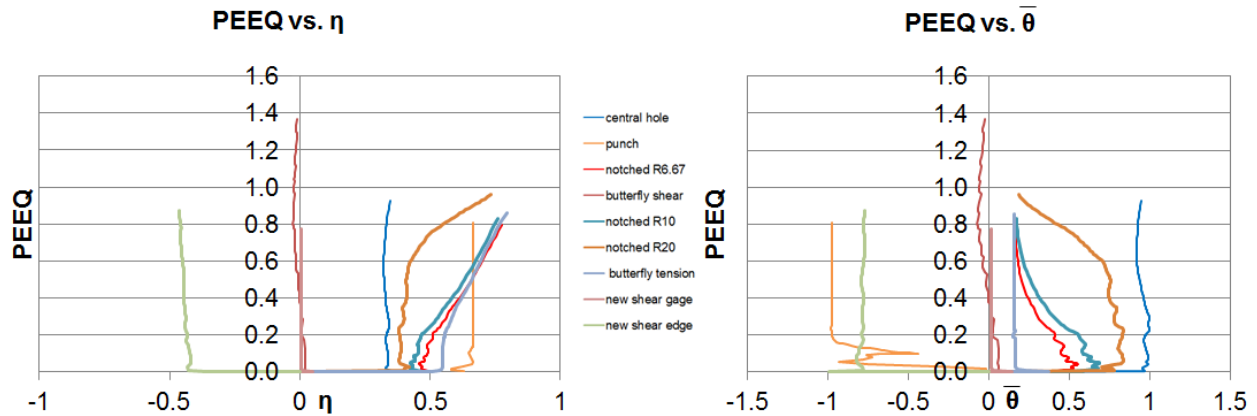


Figure 36: Plots of equivalent plastic strain as a function of triaxiality and Lode angle.

The butterfly specimen in shear buckled causing fracture to initiate early. Thus, this displacement to fracture had to be used as a conservative lower bound. A follow on study, or other studies of very ductile materials, may use an older version of the butterfly specimen which is not as good in combined loading but will be more resistant to buckling in pure shear (Figure 37). In the case of DH-36, the fracture strain was clearly linked to triaxiality and follow on tests with the older version of the butterfly specimen may show even more dependence.

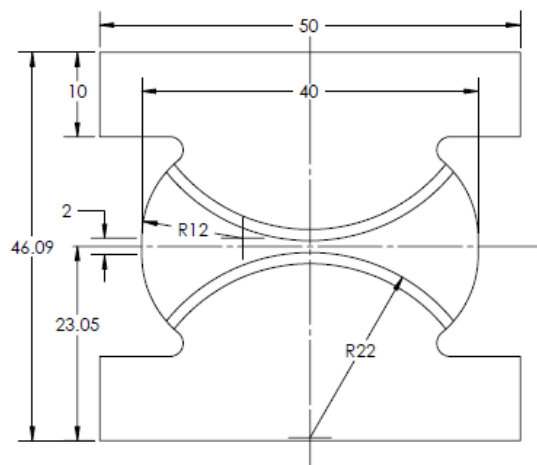


Figure 37: Alternate butterfly specimen for future testing.

### 4.3 Damage Evolution (Accumulation)

Damage evolution (accumulation) is extremely important in the actual fracture prediction. The fracture locus is defined under monotonic loading conditions; thus, the material damage ( $D$ ) is measured as:

$$D(\bar{\varepsilon}_p) = \int_0^{\bar{\varepsilon}_p} \frac{d\bar{\varepsilon}_p}{\hat{\varepsilon}_f(\eta, \bar{\theta})} = \int_0^{\bar{\varepsilon}_p} \frac{d\bar{\varepsilon}_p}{f(\eta, \bar{\theta})} \quad (20)$$

Equation 20 assumes a linear incremental relationship between  $D$  and  $\bar{\varepsilon}_p$ , with the stress parameters,  $\eta(\bar{\varepsilon}_p)$  and  $\bar{\theta}(\bar{\varepsilon}_p)$ , being unique functions of the equivalent plastic strain. Failure occurs when the equivalent plastic strain reaches the fracture strain, giving  $D(\bar{\varepsilon}_f) = 1$ . In the limiting cases when triaxiality and Lode angle are held constant over the loading cycle (the experiments used in calibration) the equation can be integrated giving:

$$\bar{\varepsilon}_f = f(\eta, \bar{\theta}) = \hat{\varepsilon}_f(\eta, \bar{\theta}) \quad (21)$$

which simplifies to all possible loading paths to fracture with constant triaxiality and Lode angle, known as the 3D fracture locus (Bai and Wierzbicki 2010). The identification of the three parameters ( $c_1$ ,  $c_2$  and  $c_3$ ) in the Modified Mohr-Coulomb criterion is achieved through the use of a Matlab code developed by the Impact and Crashworthiness Lab.

### 4.4 Fracture Parameters and Fracture Locus

The Modified-Mohr Coulomb ductile fracture criterion is based on the work of Yuanli Bai and Wierzbicki (Bai and Wierzbicki 2010). This method is also well summarized by Beese and Dunard and the presentation of this method relied heavily on their work (Beese, et al. 2010) (Dunard and Mohr 2011). The introduction to the model is outlined in Section 1.2. This section explains its development. The model is based on the observations in the original Mohr-Coulomb model, that ductile fracture is governed by maximum shear while ductility is strongly dependent on hydrostatic pressure.

$$(\tau + c_1\sigma_n)_f = c_2 \quad (22)$$

Equation 22 contains shear stress ( $\tau$ ), normal stress ( $\sigma_n$ ) and the material constants friction coefficient and shear resistance ( $c_1$  and  $c_2$  respectively). Therefore, the assumption is that fracture will occur based on a combination of normal stress and shear stress reaching a critical value on a shear plane. This is a physically sound and relatively simple fracture criterion used extensively for rock, soil, and geo-material mechanics. The somewhat lucid criterion has the necessary features describing ductile fracture, the orientation of the fracture plane, effect of stress triaxiality, and Lode angle dependence. The principal stresses in the Cartesian coordinate system were transformed to the spherical coordinate system by Bai (2008). More detail on the transformation can be found in Appendix A. The criterion can be written:

$$\bar{\sigma}_f = c_2 \left[ \sqrt{\frac{1 + c_1^2}{3}} \cos\left(\frac{\pi}{6} - \theta\right) + c_1 \left( \bar{\eta} + \frac{1}{3} \sin\left(\frac{\pi}{6} - \theta\right) \right) \right]^{-1} \quad (23)$$

The equation, in the form above, is expressed in terms of equivalent fracture stress ( $\bar{\sigma}_f$ ). It needs to be transformed into the mixed stress-strain space so that the experiments, measured in equivalent fracture strain ( $\bar{\varepsilon}_f$ ) can be incorporated. Assuming von Mises yield condition a simple power law (as seen in section 2.2.1.1)  $\bar{\sigma} = A(\varepsilon_p + \varepsilon_0)^n$ , can be used to express equivalent stress as equivalent strain, yielding:

$$\bar{\varepsilon}_f = \left[ \frac{A}{c_2} \left[ \frac{\sqrt{1 + c_1^2}}{3} \cos\left(\frac{\bar{\theta}\pi}{6}\right) + c_1 \left( \eta + \frac{1}{3} \sin\left(\frac{\bar{\theta}\pi}{6}\right) \right) \right] \right]^{-\frac{1}{n}} \quad (24)$$

Equation 24 describes a yield surface for a quadratic yield condition. A “non-quadratic” yield condition was proposed by Bai (2008) which is modified by the Lode angle parameter using the hardening law:

$$\bar{\sigma} = A\bar{\varepsilon}_n \left[ c_3 + \frac{\sqrt{3}}{2 - \sqrt{3}} (1 - c_3) \left( \sec\left(\frac{\bar{\theta}\pi}{6}\right) - 1 \right) \right] \quad (25)$$

By adding the parameter  $c_3$  various shapes of the yield surface can be formed. This feature is made clear in Figure 38, where a von Mises yield criterion is shown by  $c_3 = 1$  and a Tresca yield condition shown by  $c_3 = \sqrt{3}/2$ .

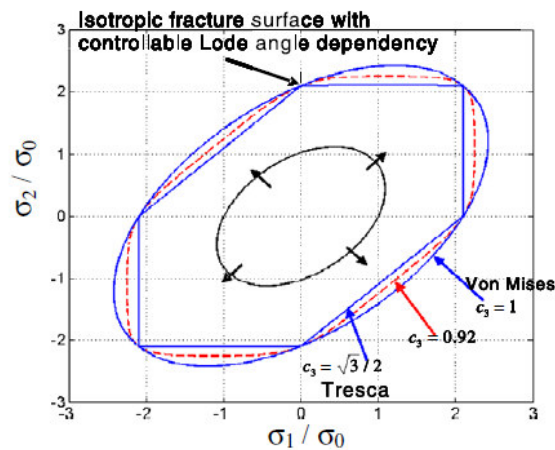


Figure 38: Effect of  $c_3$  on the yield surface (Beese, et al. 2010).

Now, with the elimination of the equivalent stress ( $\bar{\sigma}$ ) the MMC criterion becomes:

$$\bar{\epsilon}_f = \left[ \frac{A}{c_2} \left[ c_3 + \frac{\sqrt{3}}{2 - \sqrt{3}} (1 - c_3) \left( \sec\left(\frac{\bar{\theta}\pi}{6}\right) - 1 \right) \right] \cdot \left[ \frac{\sqrt{1 + c_1^2}}{3} \cos\left(\frac{\bar{\theta}\pi}{6}\right) + c_1 \left( \eta + \frac{1}{3} \sin\left(\frac{\bar{\theta}\pi}{6}\right) \right) \right] \right]^{\frac{-1}{n}} \quad (26)$$

#### 4.4.1 2D Plane Stress Model

The model can be simplified for the plane stress condition ( $\sigma_3 = 0$ ) (Wierzbicki and Xue 2005) (Bai and Wierzbicki 2008). In these cases triaxiality and Lode angle can be expressed as:

$$\xi = \cos(3\theta) = -\frac{27}{2} \eta \left( \eta^2 - \frac{1}{3} \right) = \sin\left(\frac{\pi}{2} \bar{\theta}\right) \quad (27)$$

Using this relationship, equations 26 and 27 can be combined and the plane stress fracture locus is described by:

$$\bar{\epsilon}_f = \left[ \frac{A}{c_2} f_3 \left[ \left( \sqrt{\frac{1 + c_1^2}{3}} f_1 \right) + c_1 \left( \eta + \frac{f_2}{3} \right) \right] \right]^{\frac{-1}{n}} \quad (28)$$

$$f_1 = \cos \left[ \frac{1}{3} \arcsin \left[ -\frac{27}{2} \eta \left( \eta^2 - \frac{1}{3} \right) \right] \right] \quad (29)$$

$$f_2 = \sin \left[ \frac{1}{3} \arcsin \left[ -\frac{27}{2} \eta \left( \eta^2 - \frac{1}{3} \right) \right] \right] \quad (30)$$

$$f_3 = c_3 + \frac{\sqrt{3}}{2 - \sqrt{3}} (1 - c_3) \left( \frac{1}{f_1} - 1 \right) \quad (31)$$

The parameters  $c_1$  and  $c_3$  define the contour and shape of the fracture locus and  $c_2$  adjusts the size. By assuming plane stress the problem can be solved in the 2D plane. This 2D analysis is helpful in getting a starting point if the original 3D fitting is unsuccessful. In fitting DH-36, the fracture locus has a simple shape and fitting the 3D plot was not a problem.

#### 4.4.2 3D Fracture Locus

A Matlab code, developed by the Impact and Crashworthiness lab at MIT, is used to calculate the best fit for the three parameters. The code uses the Matlab function *fmincon* which finds a constrained minimum of a function of several values. It looks for the local minimum to a solution guessed by the user using bounds also input by the user. Defining these initial conditions is where the 2D method may be useful. The function the code minimizes is defined by the difference between the experimental calibration results and the equation for the equivalent strain at fracture ( $\bar{\epsilon}_f$ ) surface. The effects of the

parameters on the fracture locus were studied in depth by Bai and Wierzbicki (2008). The calibrated 3D Modified Mohr-Coulomb fracture locus for DH-36 steel can be seen in Figure 39.

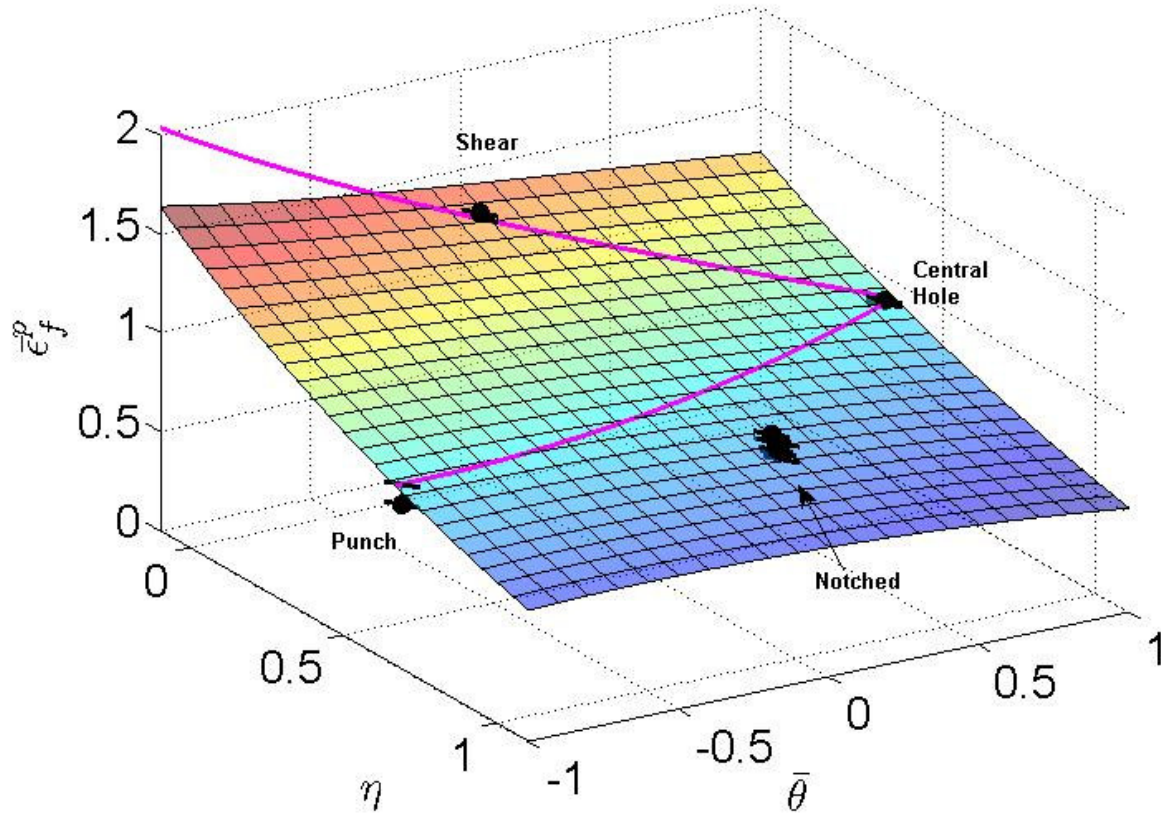


Figure 39: DH-36 MMC 3D Fracture Locus.

It is worth noting there is also a more complicated four parameter MMC model. The fourth parameter is  $c_{ax}$ . This parameter, like  $c_3$ , characterizes the dependence of the plasticity model on the first and third stress invariants. The parameter  $c_{ax}$  controls the asymmetry of the fracture envelope with respect to the plane  $\xi = 0$  (Dunard and Mohr 2011). Industry would strive for the lowest amount of parameters possible to make calibration faster and simulations less costly. With the extremely tight fit seen in Figure 39, it is clear the three parameter MMC fracture locus is sufficient for DH-36. Table 2 summarizes the MMC parameters for DH-36.

Table 2: DH-36 MMC Parameters

|                      |          |
|----------------------|----------|
| <b>A [Mpa]</b>       | 904      |
| <b>n</b>             | 0.1387   |
| <b>c1</b>            | 0.0575   |
| <b>c2</b>            | 471.2978 |
| <b>c3</b>            | 0.866    |
| <b>R<sup>2</sup></b> | .9968    |

## 5 Conclusions and Further Studies

Calibration of the Modified Mohr Coulomb fracture model for DH-36 steel was successful. There are some comments that need to be made on the results and future study. First, there was some variance seen in the basic stress strain characteristics of the material when comparing the results of this study with those of Nemat-Nasser and Guo and Yuanli Bai (Nemat-Nasser and Guo 2003) (Y. Bai 2008). It is possible that there may be differences in the material as delivered from the producer or some other outside influence to the characteristics. In agreement with the works listed, there was very little anisotropy in the material and somewhat small Lode angle dependence. The fracture strain was clearly linked to triaxiality and follow on tests may show even more dependence.

A suggestion for future execution of the calibration process would be to use even fewer specimens. The three notched specimens, 6.67, 10, and 20, and the butterfly specimen in tension give very similar positions on the fracture surface. The multiple bunched points as seen in Figure 39 do not add much more clarity to the solution and only make it more difficult for the minimization function to find a solution. For different materials these specimens may have better spacing and give a better solution to the optimization. However, if machining and testing cost is a concern one notch specimen would suffice.

Further studies may benefit from testing on the butterfly specimen in combined loading to better validate the model. Nemat-Nasser and Guo have already produced great results on DH-36 over a wide range of strain rates and temperatures (Nemat-Nasser and Guo 2003). However, further dynamic testing could make the current MMC model more robust. The Impact and Crashworthiness Lab has developed a new tool for high strain rate fracture testing which could be useful in studying DH-36 and polyurea (Dunard, Gary and Mohr 2011). As mentioned in the introduction, the motivation for calibrating DH-36 was achieving the first step in better modeling its use with polyurea. More testing of polyurea could be incorporated with these results to better optimize design and application of DH-36 with polyurea. This properly calibrated MMC model is a great first step in conducting accurate and inexpensive analysis techniques.

## References

- Abaqus. *ABAQUS analysis user's manual version 6.11*. Providence (RI): Dassault Systemes, 2011.
- Amini, M.R., A.V. Amirkhizi, and S. Nemat-Nasser. "Numerical modeling of response of monolithic and bilayer plates to impulsive loads." *International Journal of Impact Engineering*, 2010d: 90-102.
- Amini, M.R., and S. Nemat-Nasser. "Micromechanisms of ductile fracturing of DH-36 steel plates." *Int J Fract* 162, 2010c: 205-217.
- Amini, M.R., J. Isaacs, and S. Nemat-Nasser. "Investigation of effect of polyurea on response of steel plates." *Mechanics of Materials*, 2010b: 628-639.
- Amini, M.R., J. Simon, and S. Nemat-Nasser. "Numerical modeling of effect of polyurea on response of steel plates to impulsive loads in direct pressure-pulse experiments." *Mechanics of Materials*, 2010a: 615-627.
- Amirkhizi, A.V., J. Isaacs, J. McGee, and S. Nemat-Nasser. "An experimentally-based viscoelastic constitutive model for polyurea, including pressure and temperature effects." *Philosophical Magazine and Philosophical Magazine Letters*, 2006: 5847-5866.
- ASTM. "ASTM." *Standard Test Methods for Tension Testing of Metallic Materials [Metric] E 8M - 04*. 10 10, 2001. [www.astm.org](http://www.astm.org) (accessed 01 31, 2005).
- Bai, Y. *Effect of Loading History on Necking and Fracture*. Thesis, Cambridge: MIT, 2008.
- Bai, Y, and T Wierzbicki. "Application of extended Mohr-Coulomb criterion to ductile fracture." *Int J Fract* 161, 2010: 1-20.
- Bai, Y., and T. Wierzbicki. "A new model of metal plasticity and fracture with pressure and Lode." *International Journal of Plasticity*, 2008: 1071-1096.
- Bao, Y. "On fracture locus in the equivalent strain and stress triaxiality space." *International Journal of Mechanical Sciences*, 2004: 81-98.
- Bao, Y, and T Wierzbicki. "On fracture locus in the equivalent strain and stress triaxiality space." *International Journal of Mechanical Sciences*, 2004: 81-98.
- Beese, Allison, Luo Meng, Yaning Li, Yuanli Bai, and T Wierzbicki. "Partially coupled anisotropic fracture model for aluminum sheets." *Engineering Fracture Mechanics*, 2010.
- Crane, David. "U.S. Military Testing Spray-On Polymer Armor." *Defense Review*. May 10, 2004. <http://www.defensereview.com/us-military-testing-spray-on-polymer-armor/> (accessed November 02, 2011).

- Dunard, M, and D Mohr. "Hybrid experimental-numerical analysis of basic ductile fracture experiments for sheet metals." *International Journal of Solids and Structures* (International Journal of Solids and Structures), 2010a: 1130-1143.
- Dunard, M, and D Mohr. *Report 216: Predicting Ductile Fracture in Advanced High Strength Steel Sheets: Comparison of Two approaches*. Impact and Crashworthiness Lab, 2010b.
- Dunard, M., and D. Mohr. *Report No. 199: Optimized Specimen for the Fracture Testing of*. Report No. 199, Cambridge: Impact and Crashworthiness Lab, 2009.
- Dunard, Matthieu, and Dirk Mohr. "On the Predictive Capabilities of the Shear Modified Guerson and the Modified-Mohr Coulomb Fracture Models over a Wide Range of Stress Triaxialities and Lode Angles." *Journal of the Mechanics and Physics of Solids Volume 59 Issue 7*, 2011: 1374-1394.
- Dunard, Matthieu, Gerard Gary, and Dirk Mohr. *A New Device for High Strain Rate Fracture Testing*. No. 224, Cambridge: Impact and Crashworthiness Lab, 2011.
- Gurson, AL. "Continuum Theory of Ductile Rupture by Void Nucleation and Growth: Part I Yield Criteria and Flow Rules for Porous Ductile Media." *Eng. Mater. Technology*, 1977: 2-15.
- Hill, R. "A theory of the yielding and plastic flow of anisotropic metals." *Proc. R. Soc. Lond.*, 1948: 281-297.
- Johnson, G.R., and W.H. Cook. "Fracture characteristics of three metals subjected to various." *Engineering Fracture Mechanics*, 1985: 31-48.
- Kalpakjian, Serope, and Steven R. Schmid. *Manufacturing Engineering and Technology Fourth Edition*. Saddle River: Prentice-Hall, 2001.
- Klepaczko, J.R., A. Rusinek, J.A. Rodriguez-Martinez, R.B. Pecherski, and A. Arias. "Modelling of thermo-viscoplastic behaviour of DH-36 and Weldox 460-E." *Mechanics of Materials* 41, 2009: 599-621.
- Lassance, D, D Fabrègue, F Delannay, and Pardoën, T. "Mircomechanics of room and high temperature fracture in 6xxx Al alloys." *Prog. Mater. Sci.* 52 (1) (Prog. Mater. Sci. 52), 2007: 62-129.
- Matthews, William. "Army News." *Army Times*. May 03, 2004.  
<http://www.armytimes.com/legacy/new/0-ARMYPAPER-2851089.php> (accessed November 02, 2011).
- McClintock, FA. "A criterion for ductile fracture by the growth of holes ." *Transactions of the ASME, J. Appl. Mech.*, 1968: 363-371.
- Mirone, G. "Role of stress triaxiality in elastoplastic characterization and ductile failure prediction." *Engineering Fracture Mechanics*, 2007: 1203-1221.
- Mohr, D, and S Henn. "Calibration of Stress-triaxiality Dependent Crack Formation Criteria: A New Hybrid Experimental-Numerical Method." *Experimental Mechanics*, 2007: 805-820.

- Mohr, D., and M. Oswald. "A New Experimental Technique for the Multi-axial Testing." *Experimental Mechanics*, 2008: 65-77.
- Mohr, D., and M. Oswald. "A New Experimental Technique for the Multi-axial Testing." *Experimental Mechanics*, 2007: 65-77.
- Mohr, D., M. Dunard, and Keun-Hwan Kim. "Evaluation of associated and non-associated quadratic plasticity models." *International Journal of Plasticity*, 2010.
- Nasser-Nemat, S, W.J. Kang, J.D. McGee, W.-G. Guo, and J.B. Isaacs. "Experimental investigation of energy-absorption characteristics of components of sandwich structures." *International Journal of Impact Engineering*, 2006: 1119-1146.
- Nemat-Nasser, Sia, and Wei-Gup Guo. "Thermomechanical Response of DH-36 structural steel over a wide range of strain rates and temperatures." *Mechanics of Materials* 35, 2003: 1023-1047.
- "Part 2: Rules for Materials and Welding." *ABS Steel Vessel Rules*. Houston: American Bureau of Shipping, January 01, 2012.
- Rice, JR, and DM Tracey. "On the ductile enlargement of voids in triaxial stress fields." *Mech. Phys. Solids* 17, 1969: 210-217.
- Sayed, Teamer EL, Willis Mock, Alejandro Mota, Fernando Fraternali, and Michael Ortiz. "Computational assessment of ballistic impact on a high strength." *Comput. Mech.*, 2009: 525-534.
- Shim, J., and D. Mohr. "Punch indentation of polyurea at different loading velocities: Experiments and numerical simulations." *Mechanics of Materials*, 2011b: 349-360.
- Shim, J., and D. Mohr. "Rate dependent finite strain constitutive model of polyurea." *International Journal of Plasticity*, 2011a: 868-886.
- Teng, X., T. Wierzbicki, and M. Huang. "Ballistic resistance of double-layered armor plates." *International Journal of Impact Engineering*, 2008: 870-884.
- Weinberg, K., A. Mota, and M. Ortiz. "A variational constitutive model for porous metal plasticity." *Comput. Mech.*, 2006: 142-152.
- Wierzbicki, T, and D Mohr. *Research Proposal to establish the Industrial Fracture Consortium 2011-2013*. Research Proposal, Cambridge: Impact and Crashworthiness Lab, 2010.
- Wierzbicki, T, and L Xue. *Report 136: On the Effect of the Third Invariant of the Stress Deviator on Ductile Fracture*. Impact and Crashworthiness Lab, 2005.
- Xue, L. "Damage accumulation and fracture initiation in uncracked ductile solids subjected to triaxial loading." *International Journal of Solids and Structures*, 2007: 5163-5181.

Xue, L. "Stress based fracture envelope for damage plastic solids." *Engineering Fracture Mechanics*, 2009: 419-438.

Xue, Liang, Willis Mock, and Ted Belytschko . "Penetration of DH-36 Steel Plates With and Without Polyurea Coating." *Mechanics of Materials*, 2010: 981-1003.

## Appendix A: Theory – Stress States

This section assumes some background in stress mechanics. It is meant to clarify some parameters in this paper, especially because different symbols are used in the referenced literature. This section relays known mechanics knowledge but also relies heavily on the explanations in the papers of Bai and Beese (Beese, et al. 2010) (Bai and Wierzbicki 2010).

If assumed isotropic, a material can be modeled in terms of the three stress invariants of the cauchy stress tensor  $[\sigma]$ , which, as the name implies, will have the same value regardless of the coordinate system orientation. The first, second and third stress invariants of the deviatoric stress tensor  $[S]$  are defined respectively by,

$$\text{First Invariant} = p = J_1 = -\sigma_m = -\frac{1}{3} \text{tr}([\sigma]) = -\frac{1}{3}(\sigma_1 + \sigma_2 + \sigma_3)$$

$$\text{Second Invariant} = q = J_2 = \bar{\sigma} = \sqrt{\frac{3}{2} [S] : [S]} = \sqrt{\frac{1}{2} [(\sigma_1 - \sigma_2)^2 + (\sigma_2 - \sigma_3)^2 + (\sigma_3 - \sigma_1)^2]}$$

$$\text{Third Invariant } r = J_3 = \left(\frac{9}{2} [S] \cdot [S] : [S]\right)^{1/3} = \left[\frac{27}{2} \det([\sigma])\right]^{1/3} = \left[\frac{27}{2} (\sigma_1 - \sigma_m)(\sigma_2 - \sigma_m)(\sigma_3 - \sigma_m)\right]^{1/3}$$

$$[S] = [\sigma] + p[I] = [\sigma] - \left(\frac{\text{tr}([\sigma])}{3}\right) [I]$$

$\sigma_m$  is the mean stress,  $\sigma_1, \sigma_2$  and  $\sigma_3$  are the principal stresses and  $[I]$  is the identity tensor. Stress triaxiality, also known as the dimensionless hydrostatic pressure, is the ratio of the mean stress  $\sigma_m$  to the equivalent stress  $\bar{\sigma}$ .

$$\eta = \frac{-p}{q} = \sigma_m / \bar{\sigma}$$

The symbol  $\xi$  is used, for convenience, to represent the normalized third invariant.

$$\xi = \left(\frac{r}{q}\right)^3 = \cos(3\theta)$$

The dimensionless Lode angle parameter ( $\bar{\theta}$ ) is defined and used so that  $-1 < \bar{\theta} < 1$ . With  $\theta$  as the Lode angle:

$$\cos(3\theta) = (J_3 / \bar{\sigma})^3$$

$$\bar{\theta} = 1 - 6\theta/\pi = 1 - \frac{2}{\pi} \arccos(\xi)$$

The following describes the transformation of MC to the space of  $\varepsilon_f, \eta$ , and  $\bar{\theta}$  as discussed in section 4.4. The state of stress is fully defined by the principal stresses  $\sigma_1, \sigma_2$  and  $\sigma_3$ . Taking an arbitrary cutting plane, defined by the unit normal vector  $v_1, v_2$  and  $v_3$ , the shear and normal stress can be written:

$$\tau = \sqrt{v_1^2 v_2^2 (\sigma_1 - \sigma_2)^2 + v_2^2 v_3^2 (\sigma_2 - \sigma_3)^2 + v_3^2 v_1^2 (\sigma_3 - \sigma_1)^2}$$

$$\sigma_n = v_1^2 \sigma_1 + v_2^2 \sigma_2 + v_3^2 \sigma_3$$

As described above, fracture initiates when a combination of normal stress ( $\sigma_n$ ) and shear stress ( $\tau$ ) reach a critical value on a shear plane:

$$(\tau + c_1 \sigma_n)_f = c_2$$

By combining the equations for normal stress and shear stress into the equation above and maximizing the left hand side with respect to the components of the defined unit normal vector ( $v_i$ ), the orientation of the fracture plane can be found. Using the Lagrange multiplier technique, the direction cosines of the maximum, intermediate and minimum principal stresses are defined by:

$$v_1^2 = \frac{(\sqrt{1 - c_1^2} - c_1)^2}{1 + (\sqrt{1 - c_1^2} - c_1)^2}$$

$$v_2^3 = 0$$

$$v_3^2 = \frac{1}{1 + (\sqrt{1 - c_1^2} - c_1)^2}$$

By combining the six equations above the MC criterion can be described in the space of principal stresses.

As stated in Section 4.4, Bai transformed the fracture surface from the Cartesian coordinate system to the Spherical coordinate system as illustrated in Figure 40 (Y. Bai 2008).

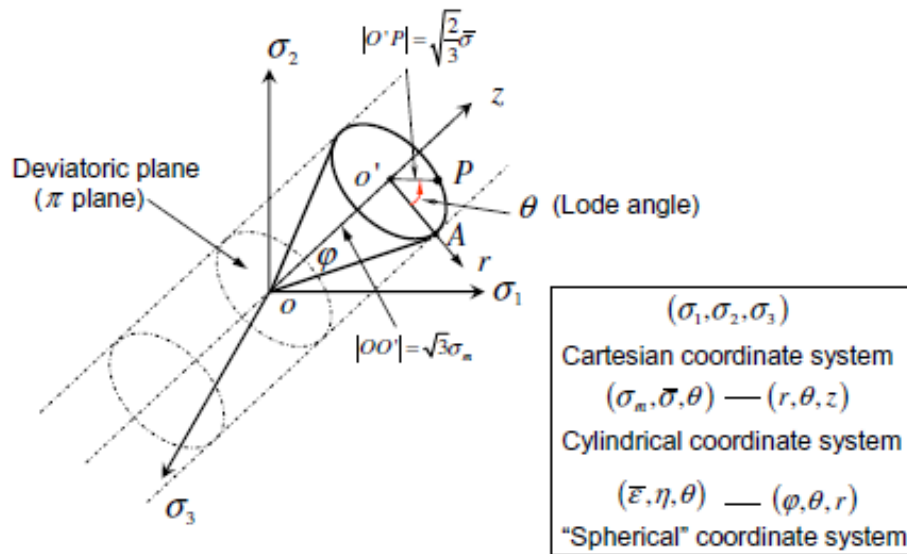


Figure 40: The coordinate systems in the space of Principal Stresses (Beese, et al. 2010) (Bai and Wierzbicki 2010)

The transformation equations are:

$$\sigma_1 = \sigma_m + s_1 = \sigma_m + \frac{2}{3}\bar{\sigma} \cos(\theta) = \left[1 + \frac{2\cos\theta}{3\eta}\right] \sigma_m$$

$$\sigma_2 = \sigma_m + s_2 = \sigma_m + \frac{2}{3}\bar{\sigma} \cos\left(\frac{2}{3}\pi - \theta\right) = \left[1 + \frac{2\cos\left(\frac{2}{3}\pi - \theta\right)}{3\eta}\right] \sigma_m$$

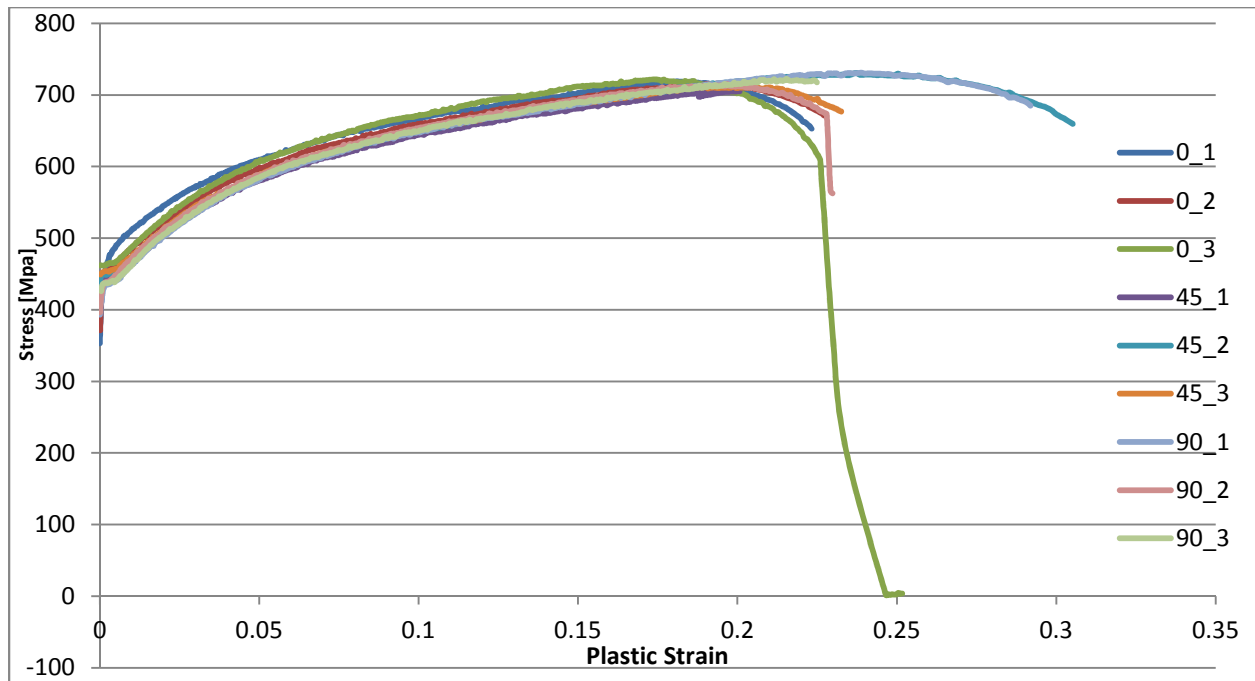
$$\sigma_3 = \sigma_m + s_3 = \sigma_m + \frac{2}{3}\bar{\sigma} \cos\left(\frac{4}{3}\pi - \theta\right) = \left[1 + \frac{2\cos\left(\frac{4}{3}\pi - \theta\right)}{3\eta}\right] \sigma_m$$

The transformed form of the MC fracture criterion, as stated in section 4.4, is:

$$\bar{\sigma}_f = c_2 \left[ \sqrt{\frac{1+c_1^2}{3}} \cos\left(\frac{\pi}{6} - \theta\right) + c_1 \left( \bar{\eta} + \frac{1}{3} \sin\left(\frac{\pi}{6} - \theta\right) \right) \right]^{-1}$$

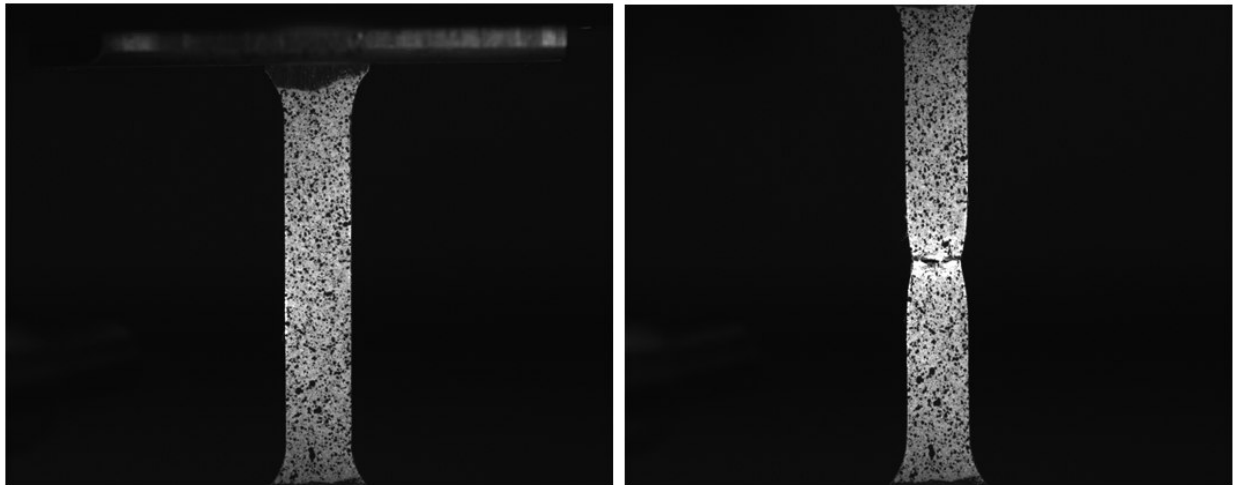
## Appendix B: Additional Data

Dog-bone stress strain curves in three directions:

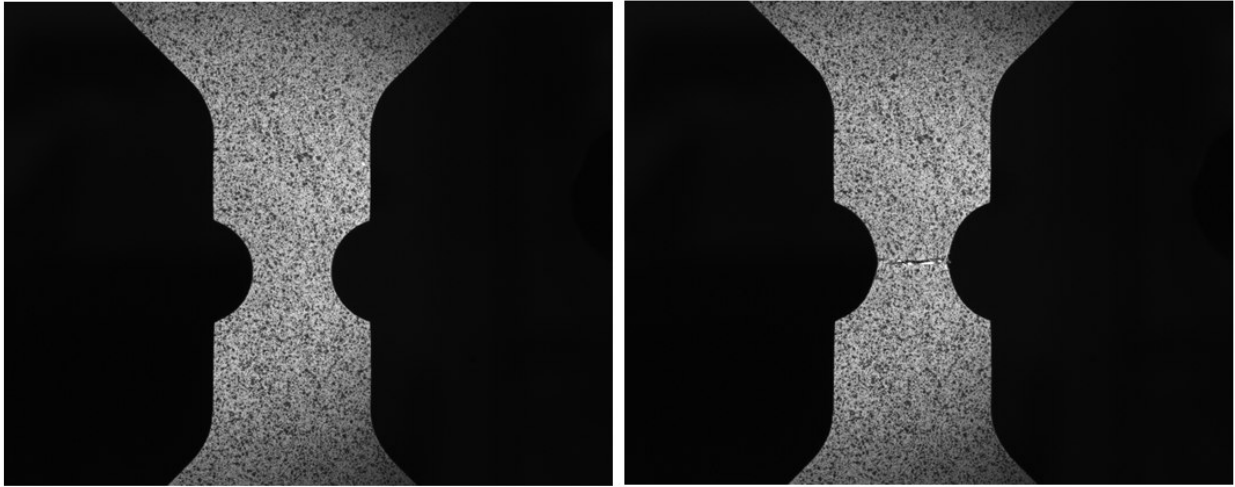


Selected before and after experiment images for each specimen:

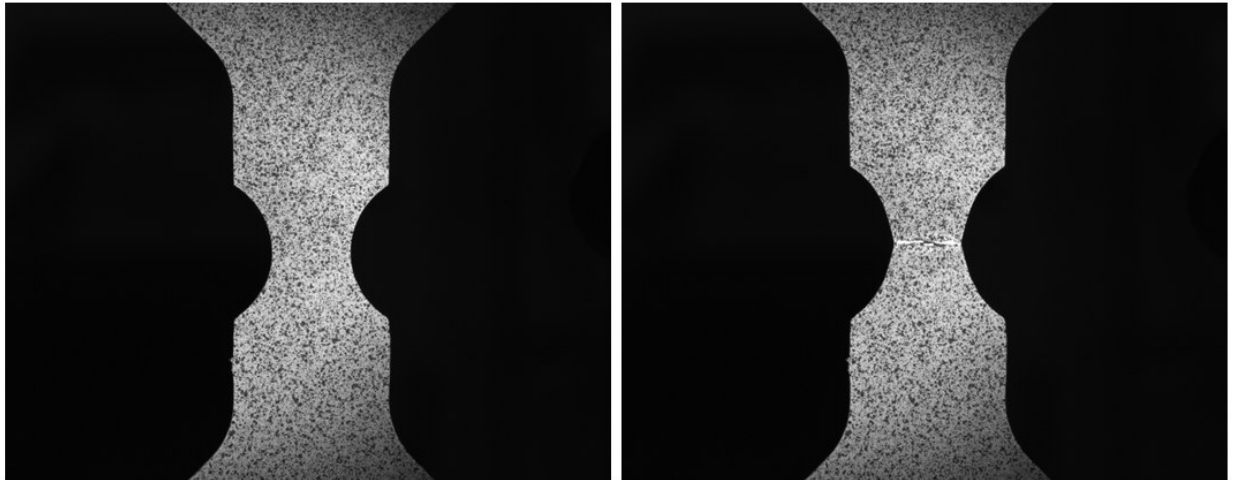
Dogbone



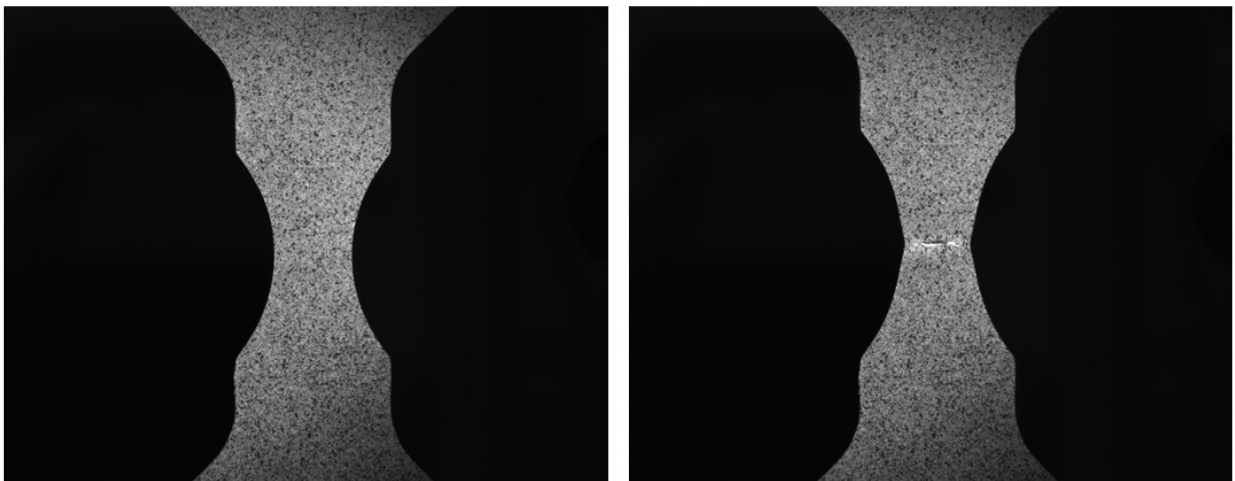
Notched 6.67



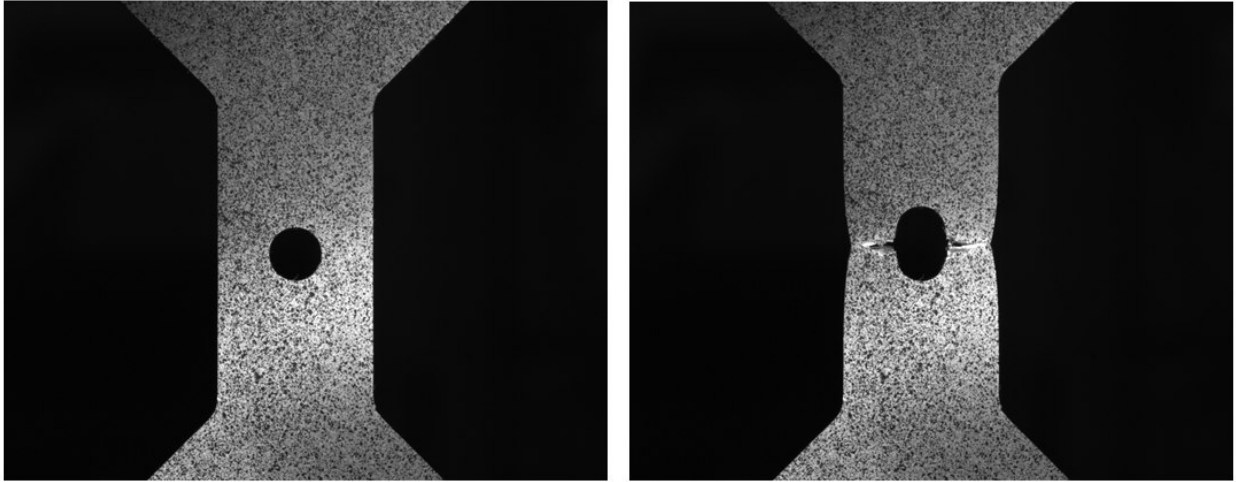
Notched 10



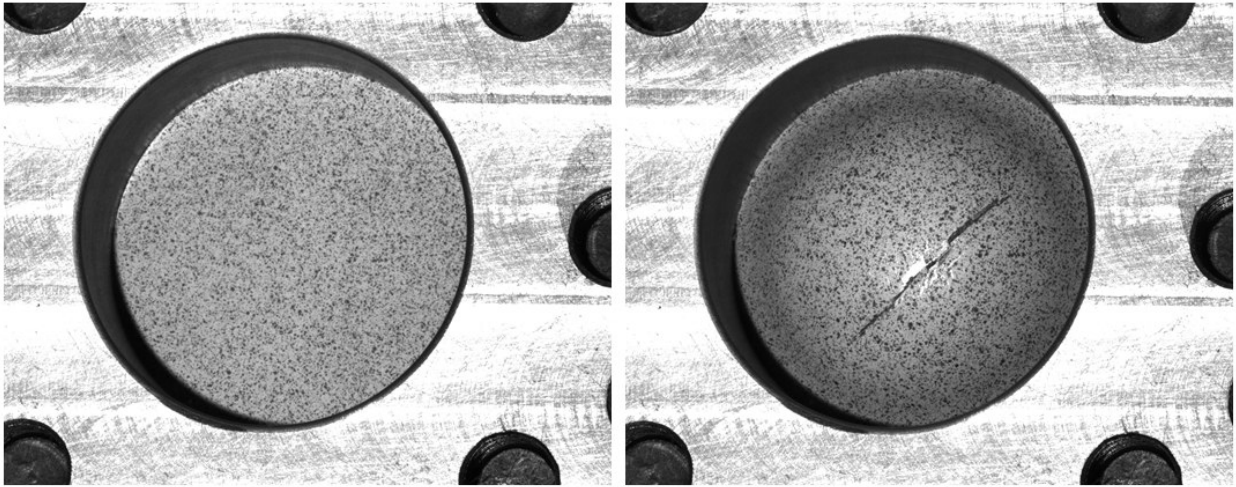
Notched 20



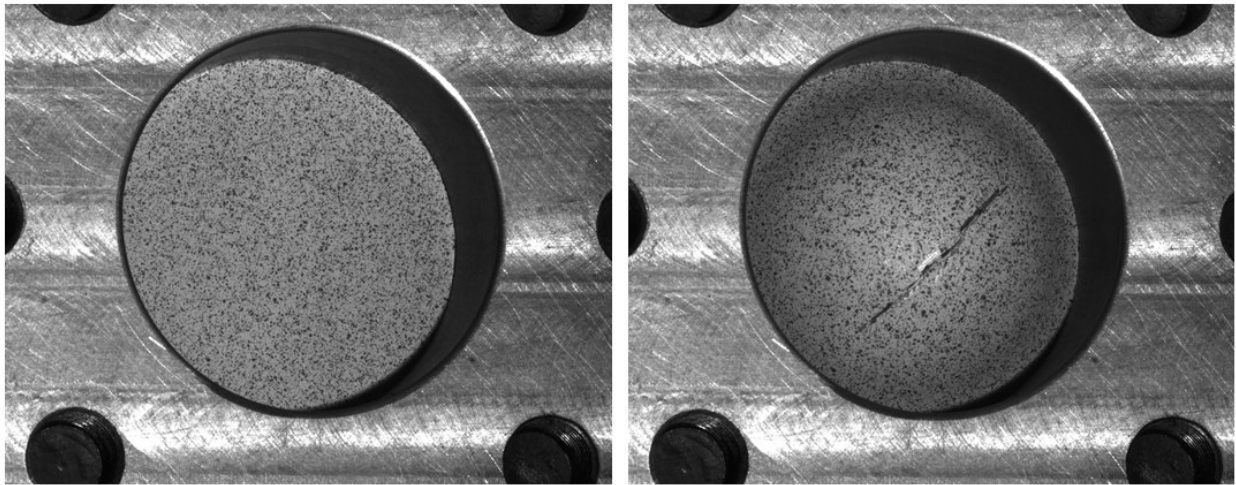
Central Hole



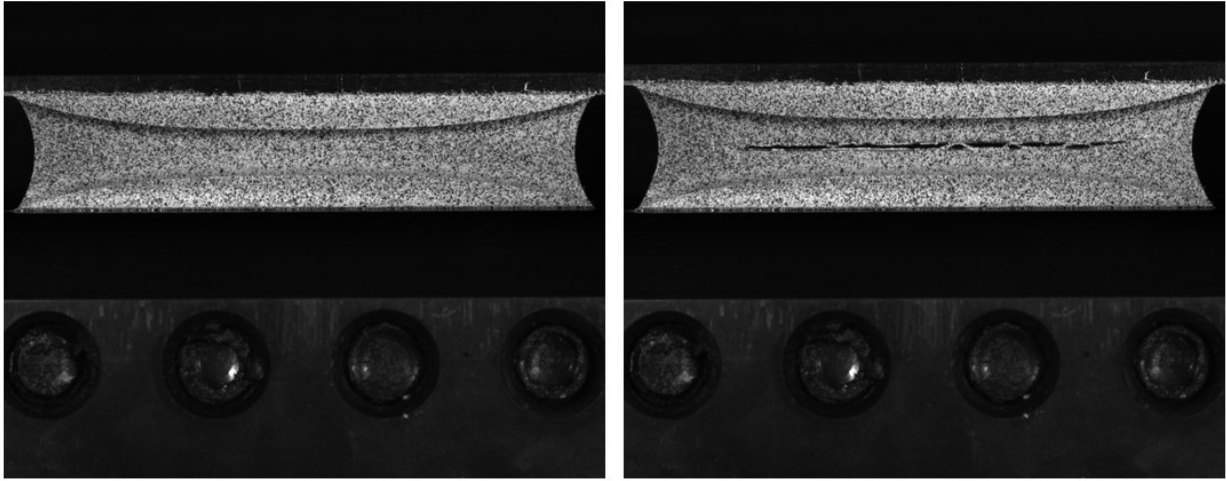
Punch View 1



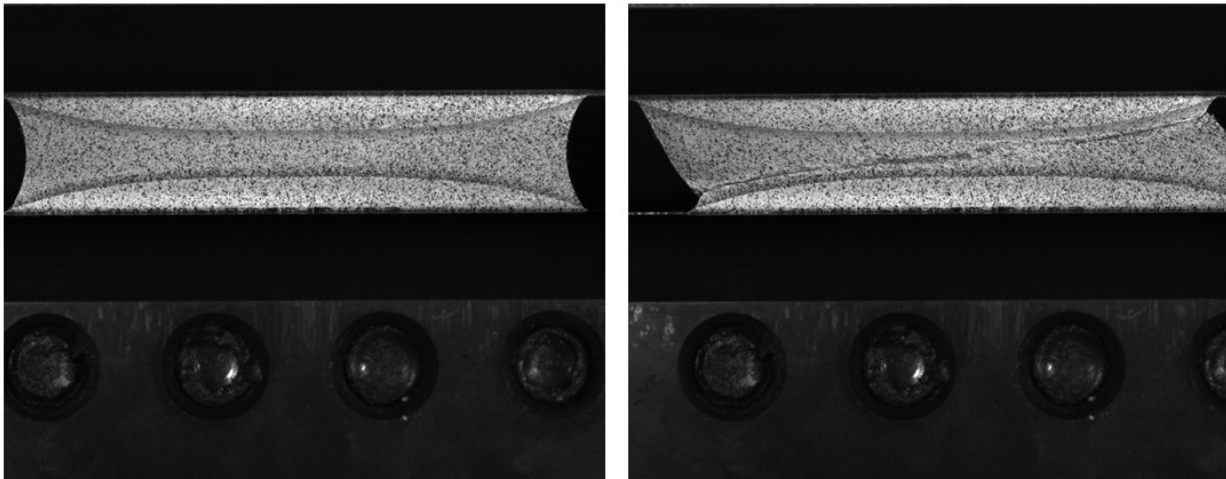
Punch View 2



Butterfly Tension

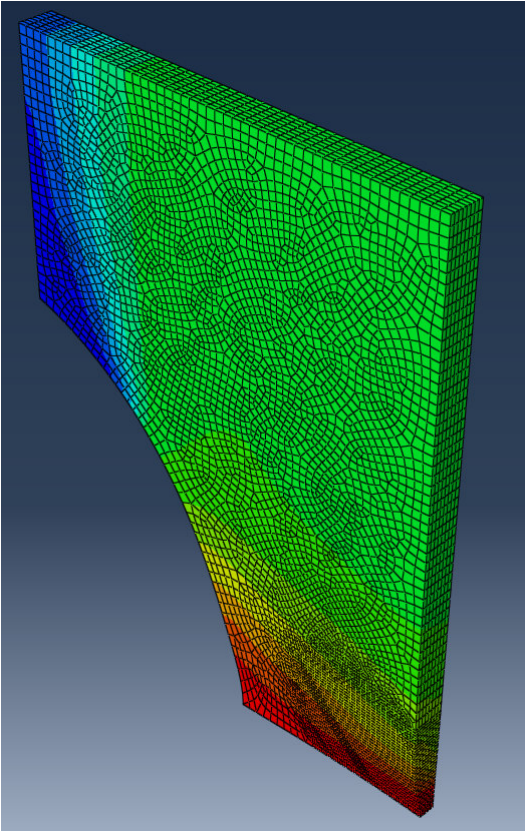


Butterfly Shear

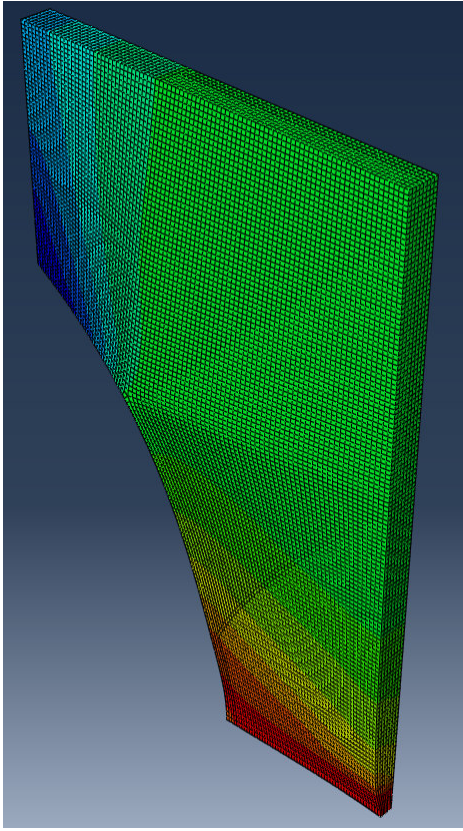


Finite Element models showing Mises stress contour plots:

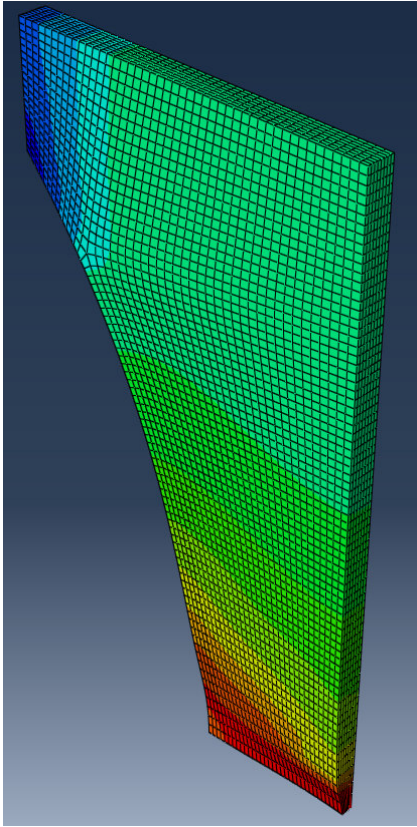
Notched 6.67:



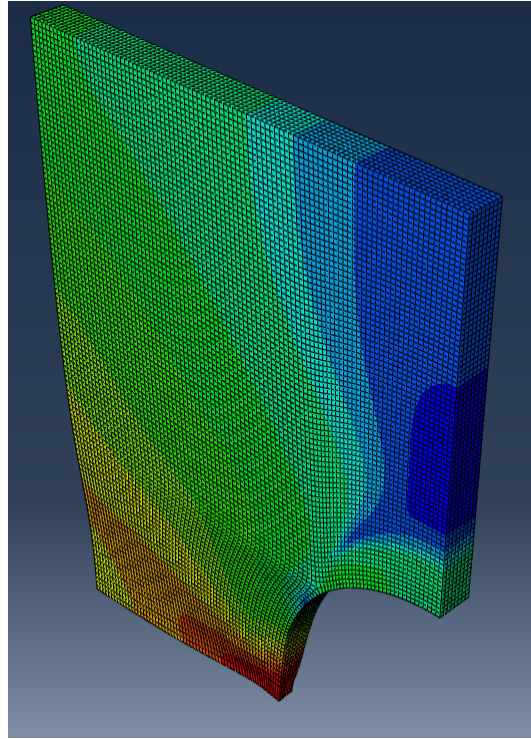
Notched 10:



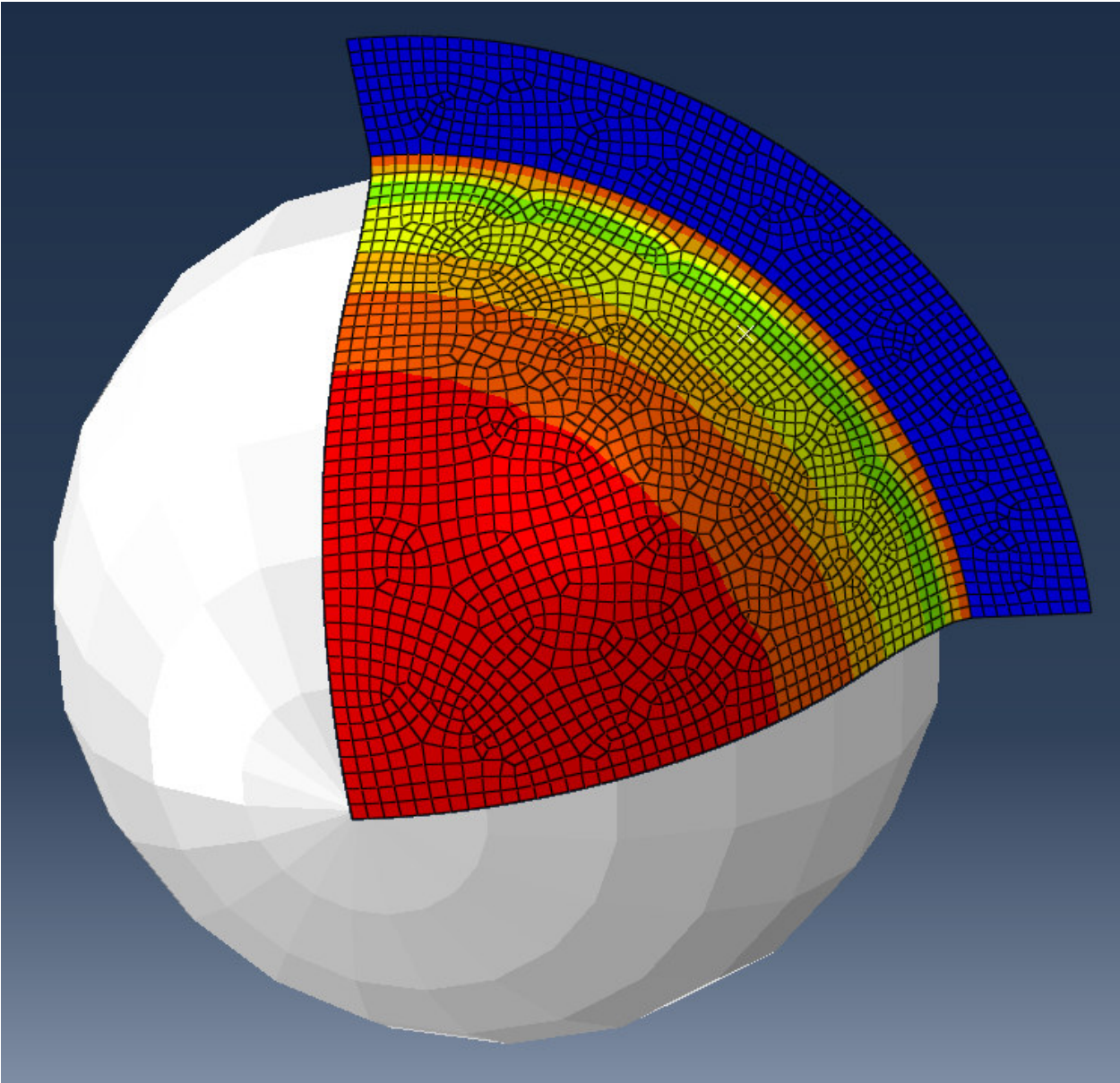
Notched 20:



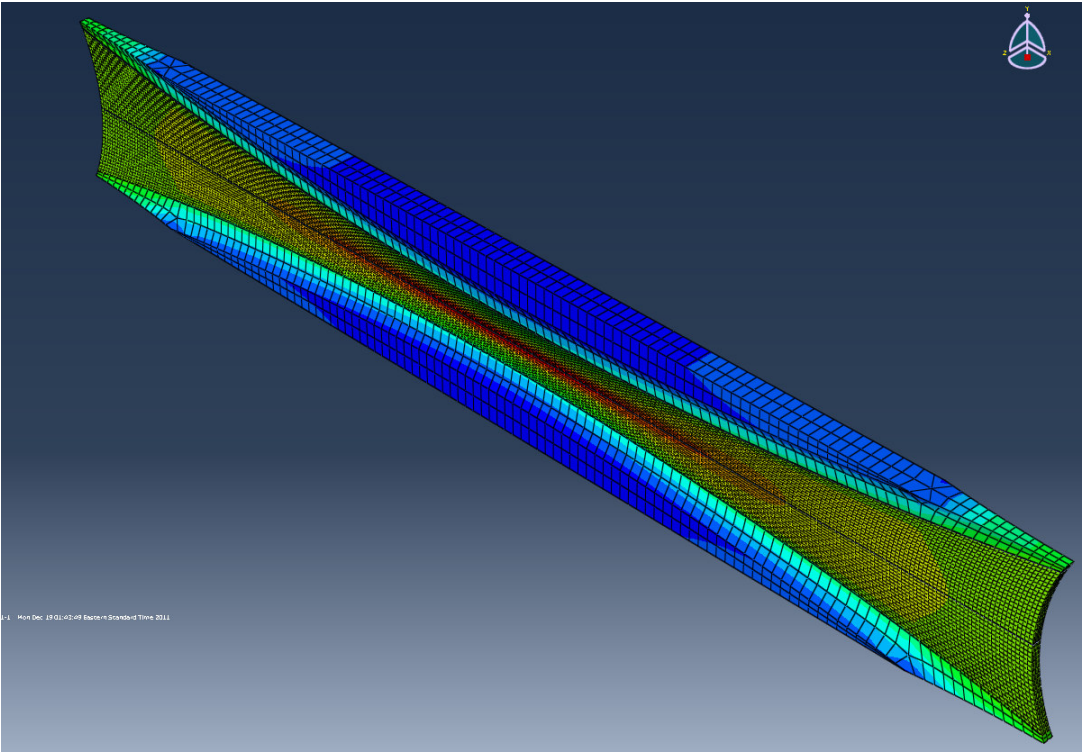
Central Hole:



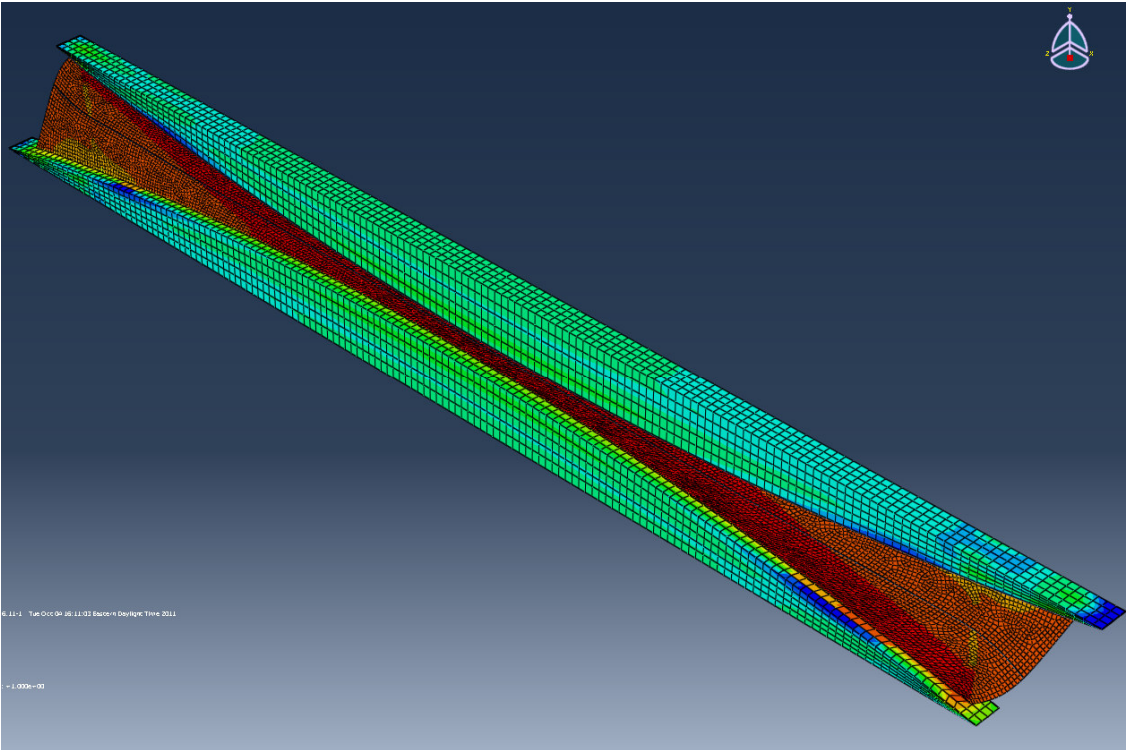
Punch:



Butterfly Tension:



Butterfly Shear:



Force displacement simulation validation (not every simulation conducted is shown on the plots):

